



# Thermal energy storage performance of liquid polyethylene glycol in core–shell polycarbonate and reduced graphene oxide fibers

Madhurima Das<sup>1</sup> · Daniel P. Ura<sup>1</sup> · Piotr K. Szewczyk<sup>1</sup> · Krzysztof Berniak<sup>1</sup> · Joanna Knapczyk-Korczak<sup>1</sup> · Mateusz M. Marzec<sup>2</sup> · Waldemar Pichór<sup>3</sup> · Urszula Stachewicz<sup>1</sup>

Received: 21 March 2024 / Revised: 12 May 2024 / Accepted: 2 July 2024 / Published online: 13 July 2024  
© The Author(s) 2024

## Abstract

Thermal energy storage is a promising, sustainable solution for challenging energy management issues. We deploy the fabrication of the reduced graphene oxide (rGO)–polycarbonate (PC) as shell and polyethylene glycol (PEG) as core to obtain hydrophobic phase change electrospun core–shell fiber system for low-temperature thermal management application. The encapsulation ratio of PEG is controlled by controlling the core flow rate, and ~93% heat energy storage efficacy is apparent for 1.5 mlh<sup>-1</sup> of core flow rate. Moreover, the prepared fiber possesses maximum latent melting and freezing enthalpy of 30.1 ± 3.7 and 25.6 ± 4.0 Jg<sup>-1</sup>, respectively. The transient dynamic temperature vs. time curve of the rGO-loaded phase change fiber demonstrates the delay of fiber surface temperature change compared to pristine fiber. We indeed show that the tunable heat transfer and thermal energy storage efficacy of phase change fiber is achieved via controlled liquid PEG delivery and the addition of rGO in shell architecture. Notably, the effectiveness of unique phase change material (PCM)–based core–shell fibers is concluded from advanced scanning thermal microscopy (SThM) and self-thermoregulation tests.

**Keywords** Core–shell fiber · Phase change materials · Thermal management · Heat transfer · Hydrophobicity

## Abbreviations

LHTES	Latent heat thermal energy storage
PCM	Phase change material
PEG	Polyethylene glycol
PC	Polycarbonate
rGO	Reduced graphene oxide
SThM	Scanning thermal microscopy
DSC	Differential scanning calorimetry
FTIR	Fourier transform infrared
XPS	X-ray photoelectron spectroscopy
IPA	Isopropyl alcohol

## 1 Introduction

In a fast-paced, high-tech global situation, the efficient cumulation and management of energy are imperative to mitigate and restrict the aggressive rate of environmental pollution and the supply and demand gap of renewable energy utilization [1]. The greenhouse gas emissions, depletion of non-renewable sources, and the increased demand for renewable energy are critical factors for environmental pollution and poor energy management–related issues due to the rapid rise in population worldwide [2, 3]. Latent heat thermal energy storage (LHTES) technology has emerged as an economically viable solution to mitigate energy crisis, atmospheric adulteration, and balancing the energy supply/demand ratio [4, 5] to create a sustainable society. The primary mechanism of LHTES technology is associated with a large amount of latent heat utilization via storing and releasing thermal energy to the surroundings during the phase transition process of phase change material (PCM) [6]. The expected market size of advanced phase change material will hit ~7.601 billion USD by 2030 with a CAGR of 17.48% during the 2021–2030 time period [7]. However, the liquid leakage of PCM during phase change, low thermal conductivity, and intrinsic rigidity of

✉ Urszula Stachewicz  
ustachew@agh.edu.pl

<sup>1</sup> Faculty of Metals Engineering and Industrial Computer Science, AGH University of Krakow, Al. A. Mickiewicza 30, 30-059 Kraków, Poland

<sup>2</sup> Academic Centre for Materials and Nanotechnology, AGH University of Krakow, Al. A. Mickiewicza 30, 30-059 Kraków, Poland

<sup>3</sup> Faculty of Materials Science and Ceramics, AGH University of Krakow, Al. A. Mickiewicza 30, 30-059 Kraków, Poland

PCM are the main drawbacks that restrict its widespread applicability in different application areas [8, 9]. Several PCM infiltration strategies have been developed to mitigate such liquid leakage complications of PCM, such as melt mixing [10], the combination of mixing and steam explosion [11], vacuum impregnation [12], cross-linking of polymer skeleton in the presence of PCM [13], micro-encapsulation [14], and so forth [15]. As Wu et al. mentioned, most of the process is strongly tied up with leakage threats at high temperatures from the porous network, constrained molecular movement of PCM inside cross-linked polymer skeleton, and complicated and extravagant synthesis procedures [16]. Recently, a wide variety of thermally conductive organic, inorganic, or hybrid fillers [8, 17, 18] has been introduced to improve the thermal conductivity of PCM and fire retardancy [19] in the composite structure, thanks to the outstanding in-plane thermal conductivity of graphene and its derivative owing to thermal transport through cross-linked  $sp^2$  bonded inter- and intra-layer structure of carbon adatom and high surface area [20–22] which is beneficial for the creation of thermally conductive PCM composite. For example, Zhang et al. reported a ~80% increment in the thermal conductivity of hydrated salt after adding ~0.018 wt.% of rGO in the composite structure [23].

Electrospinning has appeared as a popular strategy to integrate PCM into the fibrous structure to fabricate thermoregulated intelligent textiles [24]. Uni-axial and coaxial electrospinning are the scientific community's two well-known protocols for creating phase change fibers. However, the uni-axial electrospinning process possesses poor PCM encapsulation [25] and discontinuous/split phases between polymer and PCM [26], restricting its widespread applicability.

Meanwhile, coaxial electrospinning is the most optimal approach to alleviate those issues [27]. Furthermore, the high surface-to-volume ratio and flexibility of electrospun fibers [28] offer a unique form-stable platform with a high quantity accommodation of PCM inside the shell [29]. The engineered electrospun fiber with hydrophilic polymer experiences severe swelling in humid environments [30]. Therefore, developing engineered core-shell fiber with a hydrophobic shell is needed for long-term stability, which is one of the essential prerequisites for real-field implementation. Properly selecting shell polymer is a pre-eminent step for designing engineered core-shell fibers for a particular thermal management application area. Among the broad range of polymer shells employed for coaxial electrospinning processes, polycarbonate (PC) is a slowly emerging polymer because of its excellent mechanical stability, chemical resistance attributes, and hydrophobicity [31, 32]. Thanks to its rigid polymeric backbone, aromatic bisphenol A group [32] and partial double-bonded

carboxyl groups will be beneficial for fast photon transfer [33].

Organic PCM, especially polyethylene glycol (PEG), is a potential choice in a diversified field of applications owing to its low cost, biocompatibility, and tunable energy storage efficiency by adjusting its molecular weight [34, 35]. Low molecular weight PEG can change its state at near-zero or sub-zero temperatures, signifying its potential utilization in thermal management at near-zero or sub-zero temperature ranges. Furthermore, the effect of low molecular weight PEG in the presence of a PC shell or thermally conductive low-dimensional carbon-loaded polymeric shell is scarce in the literature.

Based on such consideration, we investigated the effect of low molecular weight PEG on PC, rGO:PC-based core-shell fibrous architecture towards improved heat transfer and thermal energy storage efficacy at low temperatures. Different characterization techniques, like confocal microscopy, X-ray photoelectron spectroscopy (XPS), and scanning electron microscopy (SEM), explored the inner morphology of core-shell architecture. The role of rGO addition and the impact of varying core feed rates on the thermal energy storage efficiency of the fibrous mat were also explored via a thermoregulating experiment. The effect of rGO on the thermal conduction behavior of individual PEG:PC fiber was investigated by scanning thermal microscopy (SThM). Further, we verified the fabricated fiber's thermal reliability and morphological and chemical stability.

## 2 Result and discussion

### 2.1 Morphological analysis of core-shell fibers

The encapsulation of PCM into fiber via coaxial electrospinning is one of the most popular strategies for fabricating integrated functional textiles for thermal energy storage. The perfect choice of solvent and electrospinning parameters for core and shell fluid also plays a pivotal role in obtaining a well-defined core-shell structure [27]. To investigate the effect of PEG concentration in core-shell architecture, we varied the core (PEG) flow rate from 0.6 to 1.5  $mlh^{-1}$ , keeping the shell flow rate constant at 3.9  $mlh^{-1}$ . The denotation of the sample name is followed by the flow rate of PEG, such as PEG0.6:PC, PEG1:PC, and PEG1.5:PC. To explore the effect of rGO filler, the rGO:PC as a shell (3.9  $mlh^{-1}$  flow rate) and PEG as a core (1.0  $mlh^{-1}$  flow rate) were used to create rGO-loaded phase change fiber and denoted as PEG1:PC:rGO sample. The detailed electrospinning parameters are described in Table S1. Figure 1 a–f demonstrates the PEG-loaded PC fiber with a different core flow rate. The network-like fibrous architecture was apparent for all the samples.

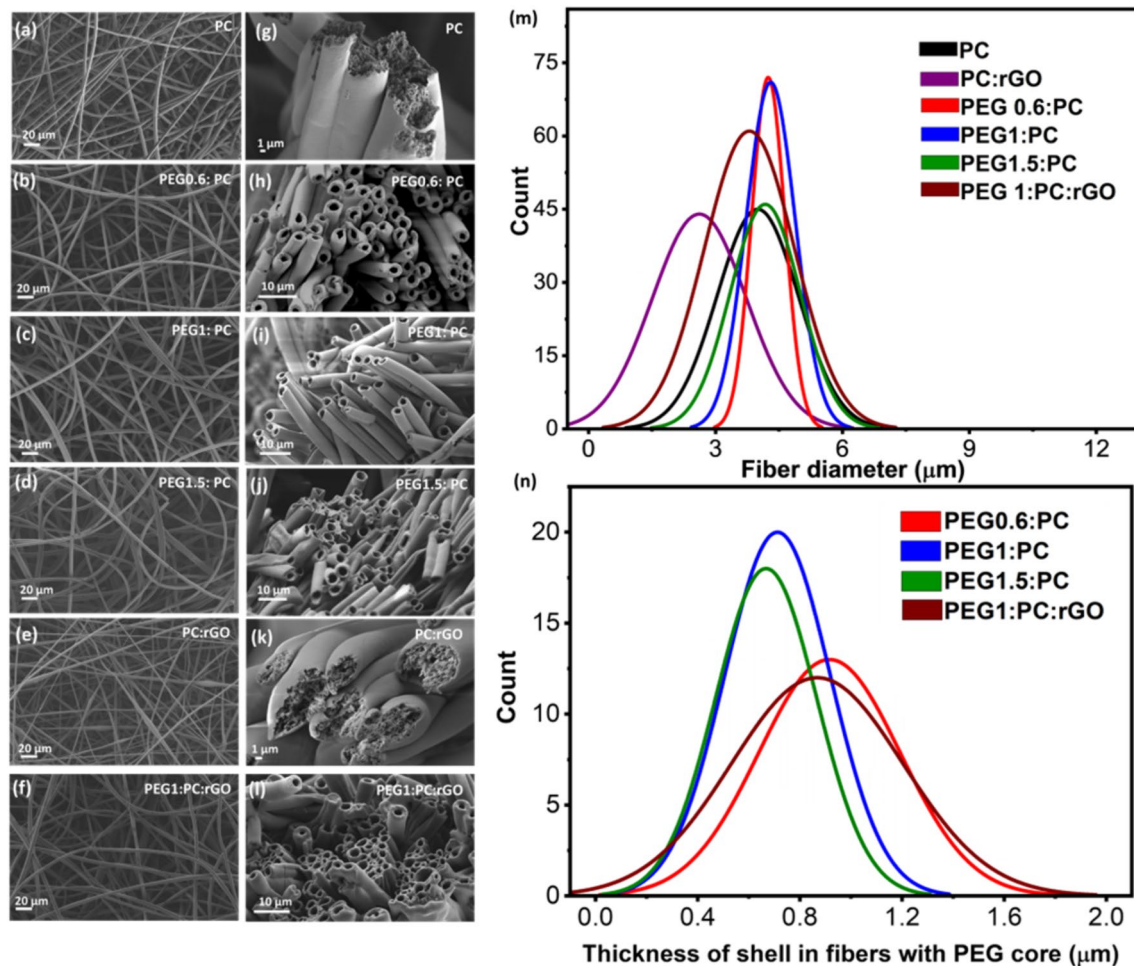


**Fig. 1** Top view SEM micrograph of electrospun mats **a** PC, **b** PEG0.6:PC, **c** PEG1:PC, **d** PEG1.5:PC, **e** rGO:PC, and **f** PEG1:PC:rGO fibers. Cross-section SEM micrograph of **g** PC; **h**

PEG0.6:PC; **i** PEG1:PC; **j** PEG1.5:PC; **k** PC:rGO; **l** PEG1:PC:rGO fibers. Distribution curve of **m** fiber diameter and **n** PC shell thickness of fibers with PEG core

The surface texture for all PEG-containing fiber mats was smooth, without any inter-fiber segregation, and similar to the surface feature of pristine PC fiber, indicating no spilling of PEG outside the fiber mat. The average fiber diameter of PC, rGO:PC, PEG0.6:PC, PEG1:PC, PEG1.5:PC, and PEG1:PC:rGO was evaluated and is presented in Table S2. The fiber diameter and shell thickness histogram after freeze-fracture for all the samples is shown in Fig. 1m and n. The wider fiber diameter distribution was observed for the PEG1:PC:rGO fiber mat compared to the pristine PEG1:PC fiber mat (see Fig. 1m). The average fiber diameter of core-shell fiber and pristine PC fiber appeared in the 3–5  $\mu\text{m}$  range (see Table S2). However, rGO-loaded fiber had a smaller diameter (see Fig. 1m and Table S2), than their pristine counterpart, which is related to the increased solution conductivity (see Table S3), causing extended jet elongation during electrospinning [36].

We chose the flake size of rGO filler within the 4–5  $\mu\text{m}$  range because of the dimensional matching between the diameters of pristine PC fiber. The dimensional compatibility will help the homogeneous distribution of rGO flakes throughout the fiber structure during electrospinning. However, finding the proof for the existence of rGO particles under SEM is challenging. Some aggregation of rGO particles was visible in the SEM micrograph (see Fig. S1(a)). We opted for light microscopy to visualize the existence of agglomerated rGO particles by analyzing the difference in color contrast between PEG:PC fibers and rGO particles. The transparent surface feature of the fiber appeared from the optical micrograph of PEG1:PC mat (see Fig. S1(b)), while several black spots were visible in PEG1:PC:rGO fiber mat (see Fig. S1(c)), signifying the presence of rGO in the composite architecture.

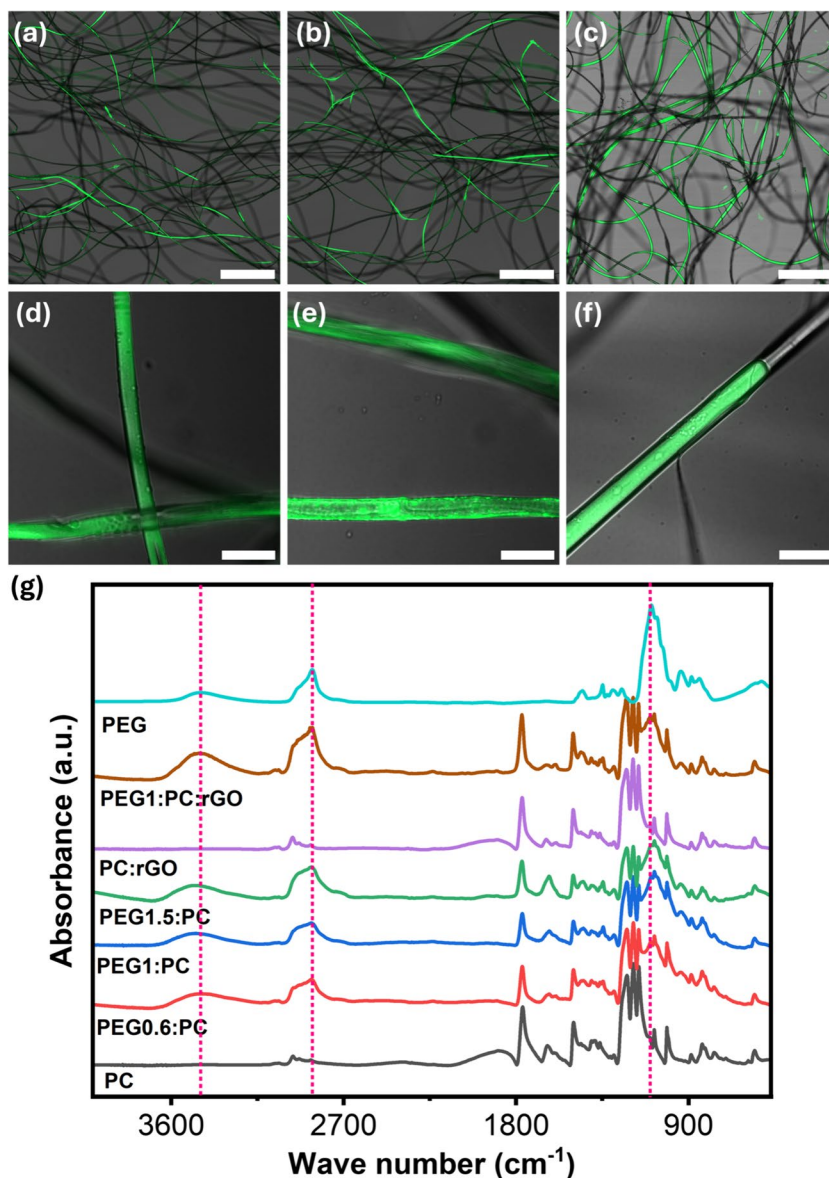
To investigate the core–shell microstructure, we also examined the cross-section image of freeze-fractured PC, PEG:PC, and PEG:PC:rGO fibers (see Fig. 1(g–l)). The cross-sectional architecture of PEG:PC and PEG:PC:rGO fibers differed remarkably from PC and PC:rGO fibers. The porous internal architecture of PC arises from vapor-induced phase separation [37] and the formation of pores caused by fast evaporation of low boiling THF solvent [38]. The cross-sectioned image of all core–shell fibers and pristine counterparts signifies the homogeneous formation of internal porous (Fig. 1g, k) or hollow architecture (Fig. 1h–j, l). The hollow morphological architecture of phase change fiber was apparent from Fig. 1h, j, and l. The fibers appear hollow solely due to the processes involved in their preparation and imaging. Initially, during the freeze-fracture process, PEG liquid is expelled into the surrounding liquid nitrogen, which does not freeze as quickly or completely within the fibers. Then, during the subsequent Au coating and SEM imaging, any remaining PEG liquid evaporates under high vacuum conditions (approximately  $10^{-4}$  Torr). These factors combined, the expulsion into liquid nitrogen and the evaporation under vacuum, cause the fibers to exhibit a hollow structure in the SEM images. From the shell thickness diameter distribution (see Fig. 1n), the core flow rate significantly influenced the shell thickness during coaxial electrospinning. The average shell thickness for PEG0.6:PC, PEG1:PC, PEG1.5:PC, and PEG1:PC:rGO fiber was evaluated and is presented in Table S4. The shell thickness marginally decreased with the increase in core flow rate from 0.6 to 1.5 mlh<sup>-1</sup>. According to Pham et al., it is caused by hydrodynamics focusing on a low core flow rate and partial pushing of the shell by increased core-flow rate owing to changes in hydrodynamics focusing on a high core flow rate. The alteration in the focus of sheath flow is the main driving force for such observation [39]. Compared to the PEG1:PC sample, the shell thickness of PEG1:PC:rGO fiber was increased. The presence of the rGO layer is responsible for the thicker shell, though the applied voltage can play a pivotal role in modulating shell thickness [40]. The distribution of PEG inside the core–shell fiber mats was investigated by the confocal imaging of fluorescein-tagged PEG/PC fiber (see Fig. 2a–f). A continuous core segment within the fiber structure was much more prominent for PC fiber with high core feed rates of 1.0 and 1.5 mlh<sup>-1</sup> than for PC fiber with a low core feed rate of 0.6 mlh<sup>-1</sup>. However, two modes of PCM distribution in the fiber structure were observed. The homogeneous evenly filled fluorescein-tagged PEG throughout the fiber was observed from the magnified fluorescence image (see Fig. 2d–f). In Fig. S2, we observed that the concentration of dye-tagged core distribution was comparatively high near the edges of the PC shell for all the electrospun samples, which is also responsible for the hollow architecture formation of phase change fiber. According to Dror et al., the three main reasons

for core attachment at the shell's edges are (a) fast evaporation of shell solvent, (b) good compatibility between core and shell, and (c) non-solvent-induced phase separation [41]. To explore the reason behind the efficient accumulation of core near the edges of the shell, we performed an adhesion and solvent miscibility test (see Fig. S3(a)) in the supporting information. The solvent miscibility test (see Fig. S3(b)) reveals that PEG is soluble in THF, DMAC, and its mixture. However, we observed a transparent gel-like texture when we added PEG with PC solution in DMAC:THF without any precipitation. Therefore, we omit the possibility of non-solvent-induced phase separation to form core–shell fiber with distinct internal features. Thus, in our case, the fast evaporation of the shell, as the flow rate was higher than for the core, and good adhesion between PC and PEG is responsible for the excellent core's attachment around the shell's edges or the mixing of core–shell liquid.

## 2.2 FTIR analysis

For pristine PC, the FTIR peaks appeared, where 1766, 1500, 1221, 1187, and 1159 cm<sup>-1</sup> correspond to C=O, phenol ring, -C-O-C group, and asymmetric and symmetric stretching of -C-O group respectively [42] (see Fig. 2g). The characteristics of FTIR peaks of all samples are shown in Table S5 in the supporting information. The C=C stretching vibration of PC arises around 1650 cm<sup>-1</sup> [43]. A peak at 2965 cm<sup>-1</sup> is associated with C<sub>sp</sub><sup>3</sup>-H stretching band [44], while the peaks at 1079 and 1013 cm<sup>-1</sup> represent -C-C-C deformation and -O-C-O stretching of PC fibers [45]. The appearance of peaks at 3445, 2864, and 1453 cm<sup>-1</sup> is associated with -O-H stretching and -CH<sub>2</sub> stretching and bending vibration of the PEG unit [46]. The peaks at 1348, 1295, and 1248 cm<sup>-1</sup> represent the characteristics of alkyl -C-H deformation peaks of PEG [47], while the peak at 1094 and 940 cm<sup>-1</sup> corresponds to -C-O-C stretching of the ether group in PEG and -CH out-of-plane bending vibrations of PEG respectively [48]. Interestingly, the presence of characteristics -O-H, -CH<sub>2</sub> stretching peaks of PEG in all core–shell PC fiber confirms the presence of PEG in the hybrid fiber structure. All characteristic peaks of both PEG and PC were observed in both PEG:PC and PEG:PC:rGO core–shell fibrous mat. No additional peaks were observed for both core–shell fiber and rGO-incorporated core–shell fiber, indicating that the structural integrity of PC was preserved even after adding PEG as core material and rGO as a filler. However, any characteristic peaks of (1 wt.%) rGO for the PEG:PC:rGO core–shell fibrous mat were not visible because they overlapped with characteristic FTIR peaks of PC and PEG (see Fig. S4).

**Fig. 2** Confocal images of fluorescein-tagged **a–c** PEG0.6:PC, PEG1:PC, and PEG1.5:PC core–shell fibers (scale bar, 200  $\mu\text{m}$ ). Magnified view of fluorescein-labeled core **d–f** PEG0.6:PC, PEG1:PC, and PEG1.5:PC core–shell fiber (scale bar, 20  $\mu\text{m}$ ). **g** FTIR of PEG-loaded PC and rGO:PC fibers



### 2.3 XPS analysis

Surface concentrations of chemical bonds obtained from fitting XPS data for all samples are listed in Table S6. Within the experiment geometry, the information depth of analysis was about 5 nm. The C 1s spectrum collected for pure PC (see Fig. 3a), sample was fitted with six lines. The first line was positioned at 284.5 eV originating from C=C  $\text{sp}^2$ -type bonds, the second line was found at 285.9 eV coming from C–C  $\text{sp}^3$ -type bonds, the third line was found at 287.3 eV indicating C–O-type bonds with carbon in the aromatic ring, the fourth line centered at 290.4 eV from the presence of O–(C=O)–O-type groups, and lines fifth and sixth were found at 291.6 eV and 292.9 eV, respectively, which are due to the shake-up process. The shake-up excitation originates from the

$\text{sp}^2$  carbon and its aromatic forms and is an additional parameter confirming the presence of this type of bond [49, 50]. For the core–shell fibers (see Fig. 3a, Fig. S5(a) and (b)). The C 1s spectra were fitted with six lines. The first line was positioned at 284.5 eV originating from C=C  $\text{sp}^2$ -type bonds and/or also C–C  $\text{sp}^3$ -type bonds, the second line found at 286.0 eV coming from C–O-type bonds in PEG, the third line found at 288.7 eV indicating C=O-type bonds, the fourth line centered at 290.4 eV from the presence of O–(C=O)–O-type groups (in PC), and lines fifth and sixth found at 291.64 eV and 292.2 eV, respectively, which are due to the shake-up process. Spectrum collected in the O 1s region (see Fig. 3b) and Fig. S5(c), (d) can be fitted with three lines: the first one centered at 532.2 eV indicating presence of C=O bonds in PC and/or C–O bonds in PEG, the second line found at

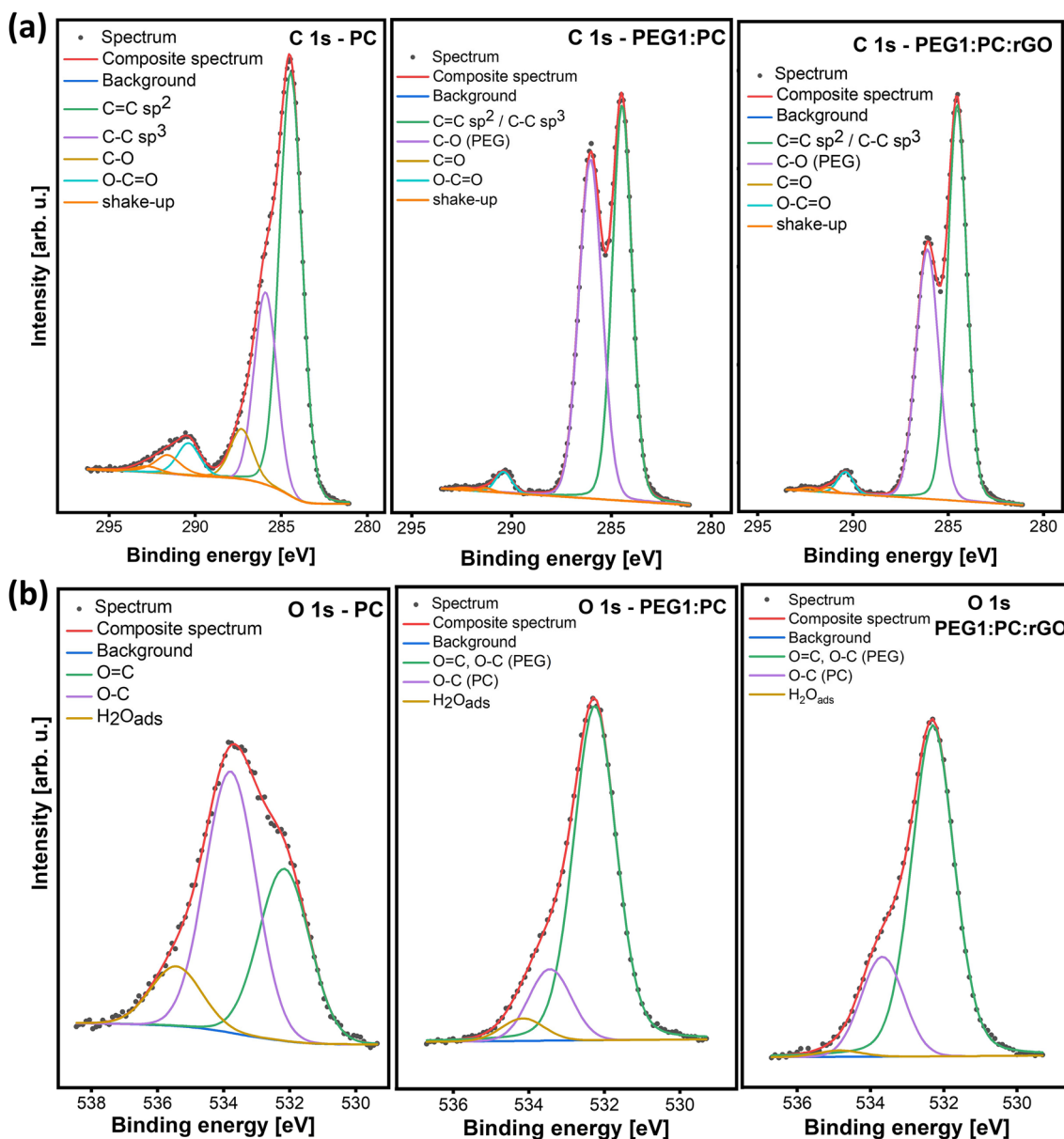


**Fig. 3** XPS data for electrospun mats. **a** C 1s spectra and **b** O 1s spectra of PC, PEG1:PC, and rGO-loaded PEG1:PC fibers

533.6 eV coming from C-O bonds from PC, and the last line centered at ~535 eV originating from adsorbed water [50, 51]. Si 2p spectra (see Fig. S5(e-i)) were fitted with doublet structure (doublet separation  $p_{3/2}-p_{1/2}$  equals 0.61 eV) with the main  $2p_{3/2}$  line centered at 102.0 eV, which indicates the presence of Si-O-type bonds [51]. The XPS results show the interfacial mixing between the core and shell during coaxial electrospinning, as PEG is partially present in the PC shell within 5-nm depth measurement. The interaction between miscible solvents (DMAC, THF with PEG) leads to the interfacial blending of core and shell components [52].

## 2.4 Wettability

The surface-wetting properties of fibers determine their environmental stability under humid conditions. The proof of core-shell fiber formation is also strongly related to surface wettability experiments, especially for hydrophobic/hydrophilic core-shell combinations. The static contact angle of pristine PC ( $135.2 \pm 4.6^\circ$ ) and PEG:PC core-shell fiber with different core flow rate ranges from 0.6 to 1.5  $\text{mlh}^{-1}$  remained similar, ranging from  $134.6 \pm 3.5^\circ$  to  $129.2 \pm 5.0^\circ$  (see Fig. 4a). From the water contact angle results, it can be stated that the surface hydrophobicity of pristine PC remains

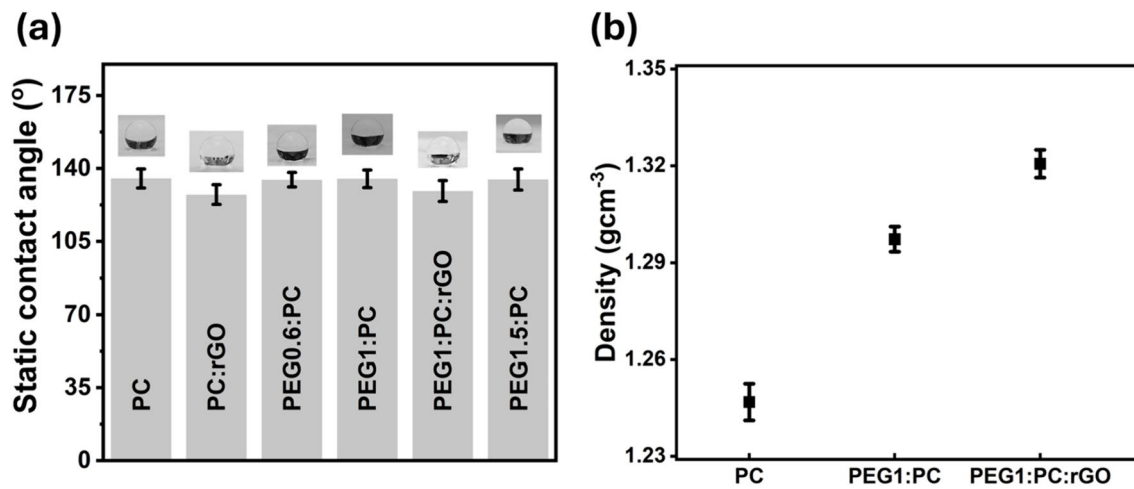


**Fig. 4** **a** The comparison of the static contact angle between PEG:PC:rGO and PEG:PC core–shell fiber with pristine counterpart. **b** The measured density of the PC, PEG1:PC, and PEG1:PC:rGO fiber mats

the same in the presence of PEG with different feeding rates, signifying the successful core encapsulation by the PC shell. The introduction of rGO slightly decreases the static contact angle values for both PC:rGO ( $127.5 \pm 4.7^\circ$ ) and PEG:PC:rGO ( $134.7 \pm 5.1^\circ$ ) fibrous mat (see Fig. 4a). Therefore, encapsulating a hydrophilic core inside a hydrophobic shell in this work gives unique advantages for long-term utilization. The oxygen-containing groups over the surface of the rGO layer are responsible for slightly reduced hydrophobicity [53]. The surface hydrophobicity of any material possesses a unique advantage over hydrophilic substances, such as promising cleaning activity [54] and minimizing the chance of bacterial adhesion [55].

## 2.5 Density evaluation

We chose three samples (PC, PEG1:PC, PEG1:PC:rGO) for density measurement to check the effect of rGO and PEG in the PC membrane (see Fig. 4b). The rise in marginal increment in measured density for the PEG-loaded sample compared to pristine PC indicates the successful loading of PEG in PC architecture. Loading rGO into PC/PEG phase change fibers leads to a marginal increased density of the fiber mat, indicating a uniform distribution of rGO within the fibrous structure. The uniform distribution of rGO can facilitate the formation of an efficient conductive pathway for better heat transfer through the membrane.

## 2.6 DSC analysis

The selection of PCM with high energy storage efficiency and excellent thermal stability under repetitive thermal cycles plays a crucial role in the long-term performance of phase change composite fibers [16]. Differential scanning

calorimetry (DSC) is an essential thermal characterization tool to investigate the above-said thermal parameters of the phase change fiber. The thermal properties of all the samples in this article were evaluated based on the second and third heating–cooling cycles. The first DSC cycle differed from other cycles for all the samples, including PEG, which is associated with two reasons. The first reason is the incomplete/partial melting/freezing of polymer chains in pristine PEG and composite PCM at first cycles and the recrystallization of residual PEG chain for the next cycle. The explanation mentioned above agrees well with the reported article by Li et al., who observed such discrepancy between first and other heating–cooling cycles for different organic PCMs [56]. The thermal contact resistance between the heat source and the sample containing crucible [56] leads to incomplete thermal equilibrium at the first cycle, because of which the shift in freezing or melting peak position was apparent. This type of phenomenon was also reported in the literature for PEG [57]. All the fabricated phase change fiber mats and pristine PEG possess both exothermic and endothermic peaks in a similar temperature region (see Fig. 5a). However, for pure PC and rGO, PC has no crystallization or melting peak at the pre-selected temperature range.

Additionally, phase change fiber's melting and freezing enthalpy increased with increasing core-flow rate as shown in Fig. 5b. The latent melting enthalpy value for PEG0.6:PC, PEG1:PC, and PEG1.5:PC fiber is  $11.24 \pm 1.57$ ,  $15.96 \pm 1.17$ , and  $30.13 \pm 3.75$  Jg<sup>-1</sup> respectively. PEG1.5:PC:rGO fiber mat possesses latent melting and freezing enthalpy of  $30.13 \pm 3.7$  Jg<sup>-1</sup> and  $25.6 \pm 3.96$  Jg<sup>-1</sup>. Electrospinning is an electrohydrodynamic phenomenon, and the latent enthalpy of phase change fiber depends on the core-feed rate, but polymer concentration also plays a pivotal role [58]. At high polymer concentration, there is

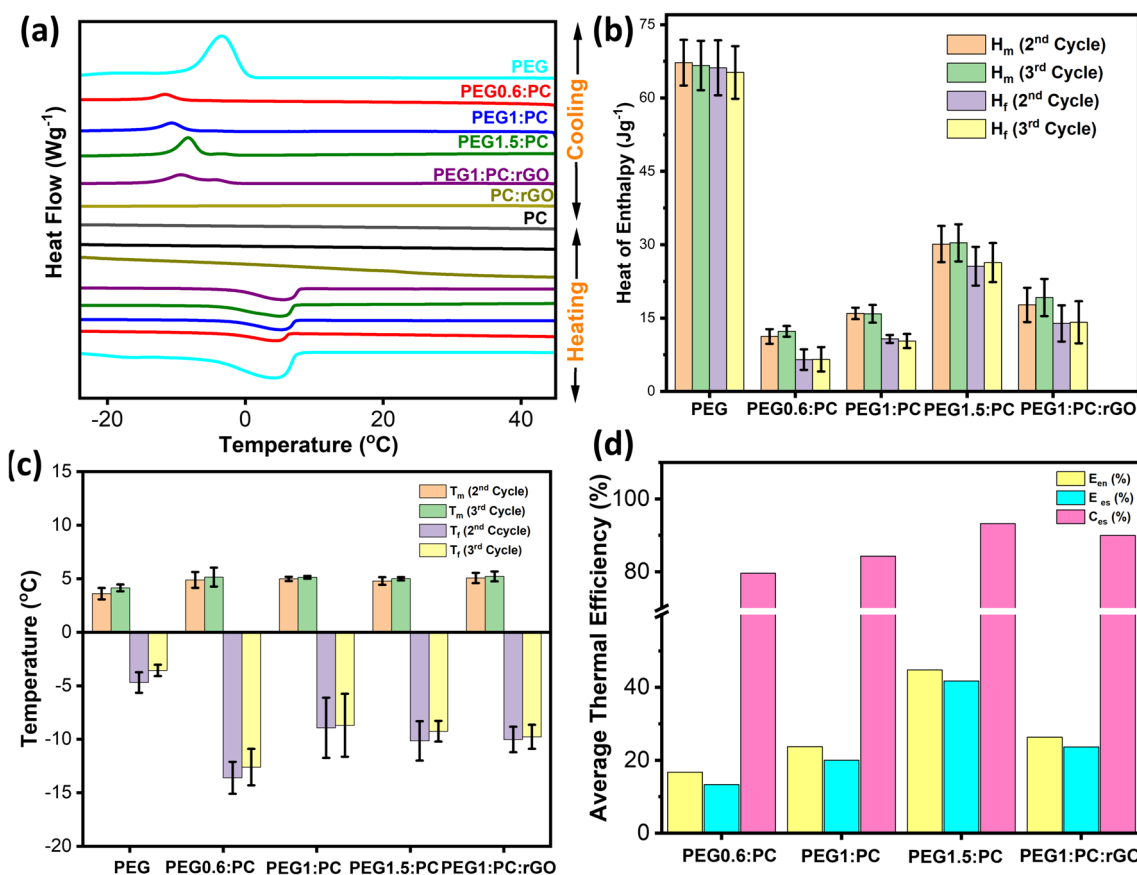


**Fig. 5** **a** DSC diagram of phase change fiber along with pristine counterpart during heating–cooling cycle, comparative bar diagram based on **b** evaluated melting and freezing enthalpy of the fiber and pristine PEG for second and third cycle, **c** evaluated melting and

freezing temperature of the fiber and pristine PEG for second and third cycle, and **d**  $E_{en}$  (%),  $E_{es}$  (%), and  $C_{es}$  (%) of all fabricated PCM fibers calculated from Eqs. (1) to (3)

no contribution of polymer towards increment in latent heat value, and often, the latent enthalpy value of core–shell fiber with different core feed rates does not follow the exponential increment trend, especially at high polymer concentration [59].

The latent heating or cooling enthalpy for all the samples did not significantly deviate from the second and third cycles, indicating the cyclic stability of all the prepared samples. However, the freezing enthalpy for all the samples was lower than its melting enthalpy. The difference in melting and freezing enthalpy of PCM and PCM-based composite depends on the values of specific heat capacity of the liquid and solid states of the composite [60].

$$\Delta H_m - \Delta H_c = \int_{T_c}^{T_m} (C_{p,l} - C_{p,s})dT \tag{1}$$

$C_{p,l}$  and  $C_{p,s}$  are the specific heat capacities of the liquid and solid for PCM and its composite;  $T$  is the temperature.

From Fig. 5c, the melting temperature of phase change fiber did not significantly change, while freezing temperature

was notably changed after the incorporation of rGO or change in core flow rate. The slight deviation of freezing temperature from second to third cycle was also apparent for all core–shell fiber mats. Interestingly, the freezing temperature of all phase change fiber mats was higher than pristine PEG. The disrupted movement of PEG in the fibrous mat is one of the main reasons for increasing the thermal parameter (freezing temperature) during the heating and cooling cycle [61]. A high amount of PEG offers an efficient nucleation pathway throughout the fibrous mat during crystallization.

The surface-induced adsorption of PEG by PC or rGO/PC, as observed from confocal microscopy, and changes in crystallinity of PEG as observed from different  $T_f$  values from DSC can be the cause of change in the thermal parameters of the composite compared to pristine PCM [62–64]. The introduction of PEG into the PC shell with a low core flow rate increased the supercooling degree (see Fig. 5c). The non-availability of crystallization sites due to a segmented portion of PEG throughout the fiber structure, as evident from confocal microscopy (see Fig. 2), is responsible for such a result. However, a further increase in the high



PEG flow rate decreased the supercooling degree, as the high amount of PEG prevents the crystallization problem. A similar trend was observed for rGO-loaded phase change fiber than pristine fiber.

The encapsulation ratio ( $E_{\text{en}}$  %), encapsulation efficiency ( $E_{\text{es}}$  %), and heat energy storage efficiency ( $C_{\text{es}}$  %) were measured by the following equations [65]:

$$E_{\text{en}}(\%) = \frac{\Delta H_{m,\text{PEGfiber}}}{\Delta H_{m,\text{PEG}}} \times 100\% \quad (2)$$

$$E_{\text{es}}(\%) = \frac{\Delta H_{m,\text{PEGFiber}} + \Delta H_{c,\text{PEGfiber}}}{\Delta H_{m,\text{PEG}} + \Delta H_{c,\text{PEG}}} \times 100\% \quad (3)$$

$$C_{\text{es}}(\%) = \frac{(\Delta H_{m,\text{PEGFiber}} + \Delta H_{c,\text{PEGfiber}}) \times \Delta H_{m,\text{PEG}}}{(\Delta H_{m,\text{PEG}} + \Delta H_{c,\text{PEG}}) \times \Delta H_{m,\text{PEGFiber}}} \times 100\% \quad (4)$$

PEG encapsulation ratio and efficiency increased with an increased PEG flow rate during production. As a result, the heat energy storage efficiency of the fiber increased from 79.57 to 93.2%. The above-observed result signifies that almost 93% of PEG can undergo phase change in contact with heat. The observed heat energy storage efficiency of our prepared material is comparable with PEG/silica-based composite (98% heat storage efficiency) [65]. Figure 5d shows that controlling the PEG flow rate enhances the PCM encapsulation ratio, encapsulation efficiency, and fiber's heat energy storage efficiency. Incorporating rGO also marginally raises latent enthalpy, PEG encapsulation ratio, and energy storage efficacy of the phase change fiber compared to pristine phase change fiber. The presence of rGO, a thermally conductive filler, induces better nucleation of PEG owing to its high surface-to-volume ratio. A similar observation is reported in the literature for rGO-loaded composite [66].

## 2.7 SThM analysis

The thermal conductivity measurement of thin film or fibrous mats is challenging by conventional methods, such as laser flash or hot disc, because of several limitations. Lack of accuracy and uncertainties in lab-scale thermal conductivity measurement for composite materials are another drawback, as highlighted by Palacios et al. [67]. Moreover, the problem of faster heat dissipation and thermal contact resistance at the junction between the temperature sensor and material is also addressed by Wang et al. [68]. The concern for the accurate measurement of thermal conductivity, especially for porous 3D architecture, is already mentioned by Codorníu et al. [69]. Fast attaining of a thermal equilibrium state, intense laser penetration depth compared to the film's thickness, and close contact between the sample and

the sample holder are additional drawbacks for the thermal conductivity measurement of the thin film [70, 71]. The carbon spraying on the sample also imparts a significant error in the thermal conductivity measurement, as mentioned in the recent report [72]. An effort has been made to measure the thermal conductivity coefficient of the phase change fiber using FOX heat flow meter. The marginal change in  $\lambda$  value for the rGO-loaded sample (see Table S7) was due to the membrane's high porosity, resulting in dominant convective heat transport through the membrane during the measurement instead of conduction. The heat scattering at the void space (with trapped air) of the membrane is another reason for the low thermal conductivity of the composite fiber. The measurement was carried out by stacking several layers of the fiber mat; thus, the air gap between layers also contributes towards heat scattering between the junctions of the layers. The researchers previously reported a marginal change in the thermal conductivity value of a hybrid fiber mat compared to the pristine one [73]. The observed experimental result is in good agreement with the above-discussed explanation. Therefore, an indirect strategy was adopted here to measure the prominent effect of rGO on heat transfer attributes of the fibrous mat by SThM, as mentioned in the recent literature report [74]. The excellent resolution ( $< 50$  nm) and high thermal sensitivity ( $< 0.01$  °C) [74, 75] are the main benefit of such an experiment. Typically, the cantilever tip was heated by an AFM laser, and the tip was moved over the sample surface using raster scanning mode. The change in temperature of the cantilever tip during the scanning of the sample surface was monitored by the attached thermocouple. The enhanced heat dissipation during tip-sample interaction signifies the better thermal conductivity of the sample, which causes rapid decrement of temperature at the tip. To investigate the effect of rGO filler on the thermal conduction behavior of phase change fibers, we performed thermal imaging on individual PEG1:PC and PEG1:PC:rGO fiber. Figure 6a demonstrates the schematic picture of the AFM tool for acquiring the SThM images of core-shell fiber along with SThM and topographic micrograph images (see Fig. 6b–g) of individual fibers from PEG1:PC and PEG1:PC:rGO. The lower surface temperature of the material signifies rapid heat conduction attributes of the material during AFM tip-sample interaction. The SThM images show higher thermal transfer for fibers loaded with rGO than PEG:PC fiber. A significant temperature drop is observed in Fig. 6g for agglomerated rGO flakes at the corner of core-shell fiber, signifying its excellent thermal conduction attributes. Figure 6h represents the bar diagram of the average surface temperature of the fiber along with the background temperature. From Fig. 6h, we observed that the background temperature for both samples is stable and similar ( $42.22 \pm 0.16$  °C and  $42.54 \pm 0.08$  °C), indicating a homogeneous temperature distribution profile. On average,

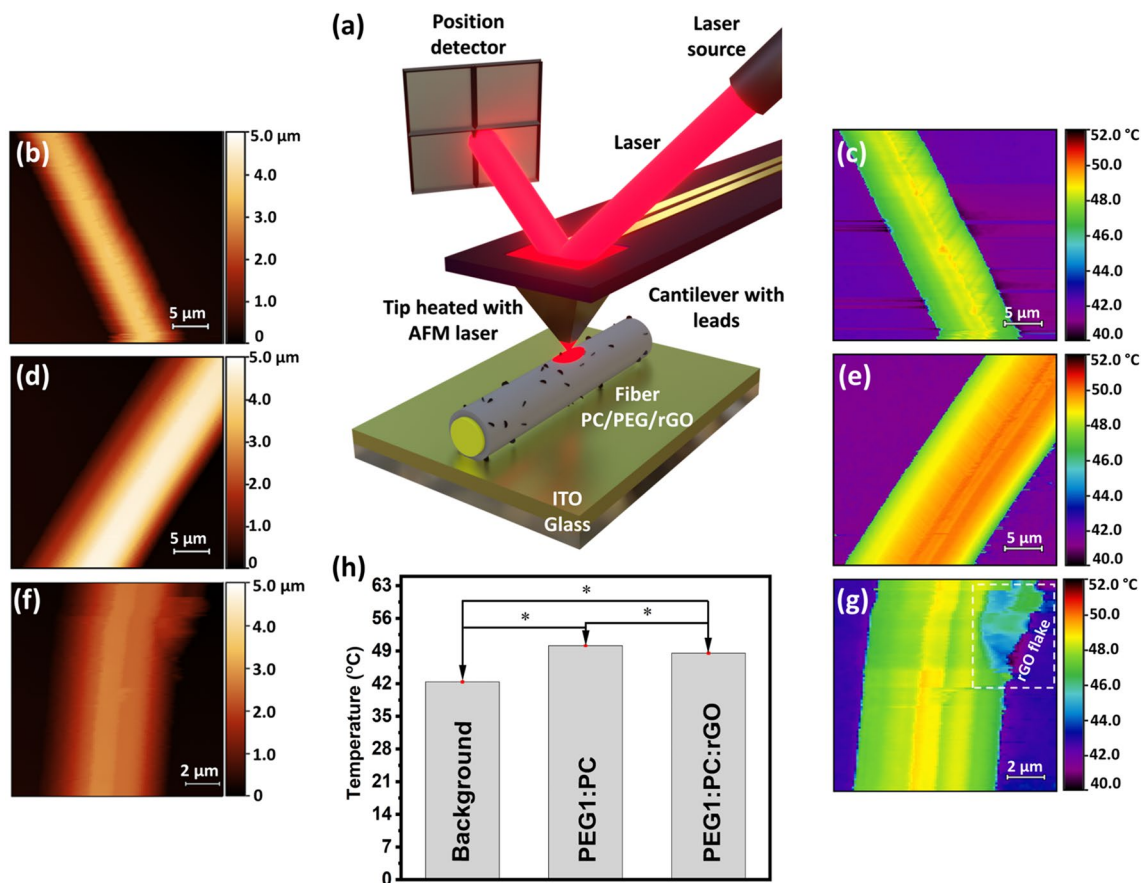


**Fig. 6** **a** The schematic picture of the AFM tool for acquiring the SThM images of core-shell fiber along with **b** topographic and **c** SThM image of PEG1:PC:rGO single fiber. **d** Topographic and **e** SThM image of PEG1:PC single fiber. **f**, **g** Topographic and SThM image of PEG1:PC:rGO fiber indicates the attachment of rGO flakes

on the surface of the core-shell fiber. **h** The comparative study on the increment of temperature with and without rGO-loaded PCM fiber under laser irradiation taking background as a control. \*Statistical significance calculated with a two-sample *T*-test, significant level 0.05; error bars are based on standard deviation

the PEG1:PC fibers had a temperature of  $50.13 \pm 0.10$  °C compared to  $48.52 \pm 0.16$  °C for PEG1:PC:rGO fiber. An average surface temperature decrement of  $\sim 2$  °C suggests that the rGO-loaded phase change fiber exhibited improved thermal conductivity compared to the pristine phase change fiber. The statistical significance test also agreed with the experimental result. The homogeneous distribution of rGO in the fiber matrix and low interfacial thermal resistance between PC and rGO owing to  $\Pi$ - $\Pi$  stacking association is likely the reason for better thermal conductivity of rGO-loaded phase change fiber [76].

## 2.8 The self-thermoregulation performance analysis of fibrous mat

Choosing relevant phase change temperature with high phase change enthalpy impacts the performance of electrospun PCM fibrous mats for a particular thermal management application. The self-thermoregulation performance of the fabricated mat was investigated by monitoring the

temperature evolution using an infrared camera. A thermal camera was employed to record the temperature changes of the fibrous membrane after exposing the frozen fiber membrane on the Styrofoam plate to room temperature from the freezer ( $-24$  °C). From the thermal camera result shown in Fig. 7a, we plot the temperature vs. time curve (see Fig. 7b). The digital photograph of a Styrofoam plate with fiber samples is shown in Fig. 7b, inset. A rapid increase in temperature was observed for all the fiber mats during the first 150 s, and later, it slowed down. The rapid increase in temperature occurred due to sudden changes in the temperature between the inside and outside of the freezer. From the curve in Fig. 7c, we noticed the delay of increment in surface temperature of PCM fibers, which was high compared to PC fiber up to 600 s. The faster warm-up of fiber was followed for rGO-loaded phase change fiber in correlation to pristine core-shell fiber. Almost 2 °C decrement in temperature rise was observed for PEG1.5:PC fiber compared to pure PC fiber mat. The delay in incrementing surface temperature of all fiber mats kept in the freezer for 2 days was calculated

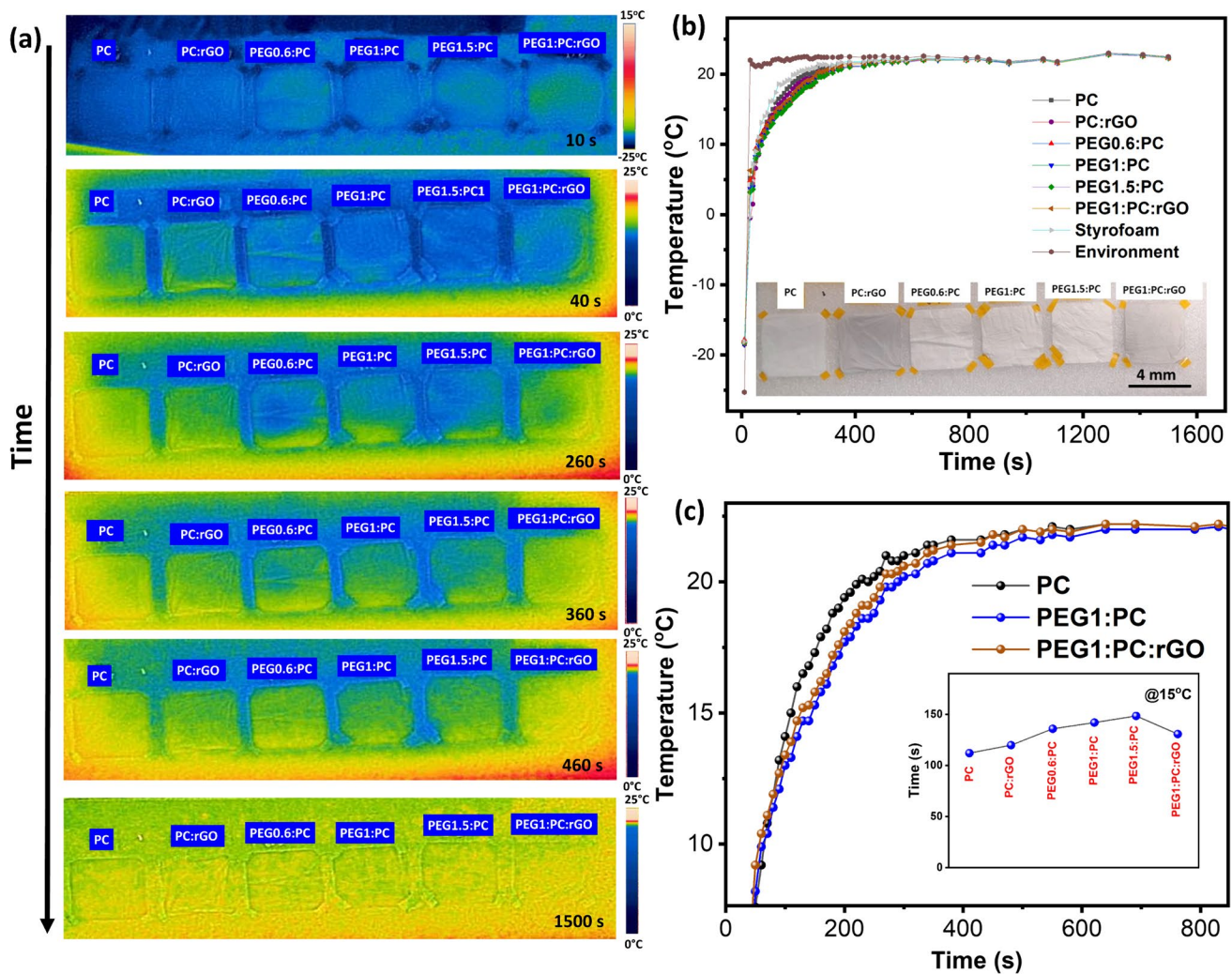


**Fig. 7** **a** Thermal camera images of all fabricated PCM fibers during the thawing experiment at room temperature at a different time interval. **b** Temperature vs. time curve of all fabricated PCM fibers during the freezing–thawing experiment (inset: images of arranged fiber mat samples on a Styrofoam plate, used in the investigation).

and is represented in Fig. 7c, inset. A high PEG loading results in more delayed increments in the fiber’s surface temperature. For example, pristine PC took 112 s to reach 15 °C, but PEG1.5:PC took 148 s when the fiber mat was kept in the freezer for 48 h. rGO-incorporated PEG1:PC fiber took 130 s to reach 15 °C, while PEG1:PC fiber took about ~140–142 s, respectively. This measurement signifies that rGO in core–shell fiber heightens the fiber surface temperature owing to its high thermal conductivity. The experimental result obtained from SThM and thermal conductivity coefficient analysis also agrees with the above statement.

However, the time delay in reaching a particular temperature is higher for rGO:PC fibers than PC fibers. As observed from the cross-section image (see Fig. 1), the porous and compact architecture of PC:rGO fibers causes phonon

**c** The magnified temperature vs. time curve of PC, PEG1:PC, and PEG1:PC:rGO fiber showing the difference in increment of temperature with time (inset: a comparative bar diagram that demonstrates the time taken for each fiber mat to attain 15 °C during the freezing–thawing experiment)

scattering with a poor connection between rGO flakes, resulting in weak heat transport. The porous architecture-induced heat carrier scattering phenomenon agrees well with the above-said explanation [77]. We did not notice a broader plateau effect of PCM from the temperature vs. time curve. According to Li et al., temperature lag between the environment and fibrous mat possesses a vital role in the heat absorption efficacy of the PCM fabric, which is responsible for such an effect [78]. After exposing the fiber from –24 °C to room temperature, there was a ~47 °C temperature difference between the fibrous mat and the environment. Therefore, PCM’s high heat absorption power yields complete phase transformation quickly without showing any broader plateau, as in previous reports [79]. Moreover, we performed another control experiment to investigate whether

a similar cooling effect happened at the different portions of the Styrofoam (see Fig. S6(a–e)) in the supporting information. From thermal camera images (see Fig. S6(a–c)), all fibers placed at the different positions on the Styrofoam are heated gradually. The temperature vs. time curve (see Fig. S6(d)) demonstrated a similar parabolic curve trend with minimal change in temperature rise for all the PC fibers at different positions. The obtained result signifies the homogeneous temperature distribution at the various places of the Styrofoam (see Fig. S6(d)) in the supporting information. This observed result cancels out the possibility of different surface temperatures of Styrofoam (at different positions induced thermal measurement error. The surface temperature evaluation technique from the thermal image is shown in Fig. S6(e).

The role of rGO inside the fibrous mat is to offer a fast heat transfer process to achieve the heating or cooling phenomenon faster. The thermal conductivity of the PC is not adequate for transferring heat from the surroundings to the core. Therefore, it is imperative to add thermally conductive filler in the shell.

The low thickness of the mat (the thickness of the mat varies ~150 to 340  $\mu\text{m}$ ), as shown in Fig. 8a, is responsible for marginal surface temperature (about 2  $^{\circ}\text{C}$  delay) change compared to pristine PC fiber. The average range of 17–30 fibers is present across this thickness zone in the mat, as shown in Fig. 8a, inset. The insufficient number of phase change fibers along this thickness zone and the low thickness of the mat are responsible for such results. Furthermore, an effort had been made to compare our obtained result with the literature report based on the thermal properties of the PCM composite associated with phase transition at near-zero or sub-zero temperature zone (see Fig. 8b). The result shows

that our fabricated fiber's latent enthalpy value is comparable to or even better than PAN/IPP, multicomponent phase change fiber, and PEG-based film. Our result is also better than that of PEG-based film and PAN/PEG-based fiber in supercooling degrees [79, 82]. However, the mat's thickness in the PAN/PEG-based system (1 mm) is higher than ours (see Fig. 8a), and the duration of electrospinning and thickness of the fiber mat are not available for most of the literature reports. Indeed, the increment of electrospinning time or a layered-based compressed system can significantly improve the heat storage efficacy of the fiber mat. Table S8 demonstrates that our results from the thermoregulation experiment are similar or even higher than those previously reported literature. However, the common drawback of the reported literature is the non-availability of sufficient data like thickness mat or deposition time of mat produced via electrospinning, which makes it very difficult to compare and validate for real-life applications. The intended application area of such newly fabricated textile material lies in cold energy storage application, specifically, thermal management while transporting medicinal products and foods. A lot of medicinal products need to be preserved under the 2–8  $^{\circ}\text{C}$  temperature range [83]. The optimum preservation temperature for fresh vegetables and fruits ranges from 5 to 15  $^{\circ}\text{C}$  [84]. On the other hand, the freezing zone of our phase change fiber mat can be utilized for the comfort of trekkers, especially at night in mountain areas or frigid regions.

To investigate whether there is any effect of porosity towards self-thermoregulation behavior of phase change fiber mat, the porosity of the fiber membrane was evaluated from the alcohol uptake method. The equation for the theoretical calculation of the membrane porosity ( $P$ ) is given below [85]:

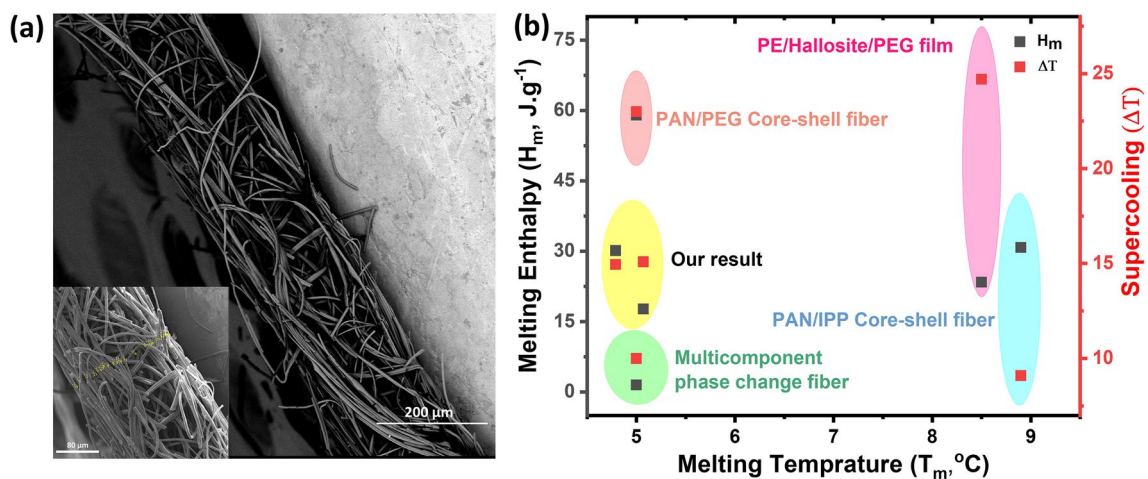


**Fig. 8** **a** Thickness of PEG1:PC:rGO fiber mat (inset: the calculation of total fiber number from the top view). **b** The comparison of our developed phase change fiber with the literature report [79–82] asso-

ciated with PEG-based film/phase change fiber fabricated to investigate thermal energy storage efficacy at near-zero temperature

$$P = \frac{\frac{M_{\text{IPA}}}{\rho_{\text{IPA}}}}{\left(\frac{M_{\text{IPA}}}{\rho_{\text{IPA}}} + \frac{M_{\text{m}}}{\rho_{\text{P}}}\right)} \quad (5)$$

where  $M_{\text{m}}$  is the weight of membranes,  $M_{\text{IPA}}$  is the weight of the absorbed IPA by membranes,  $\rho_{\text{P}}$  is the overall density of used raw materials, and  $\rho_{\text{IPA}}$  is the density of IPA ( $0.786 \text{ g cm}^{-3}$ ). The measured density of PC, PEG1:PC, and rGO-loaded PEG1:PC samples is  $1.2468 \pm 0.0057$ ,  $1.2972 \pm 0.0038$ , and  $1.3206 \pm 0.0043 \text{ g cm}^{-3}$  respectively (see Fig. 4b). Therefore, the calculated porosity for PC, PEG1:PC, and rGO-loaded PEG1:PC samples was  $86.19 \pm 1.24\%$ ,  $76.24 \pm 1.47\%$ , and  $81.11 \pm 1.34\%$ , respectively. In general, the increase in porosity of the material causes a decrease in thermal conductivity and improves thermal insulation attributes [86, 87]. However, as expected from the evaluation, the reverse trend signifies that porosity does not significantly affect the fiber mat's thermoregulation efficacy. In conjugation, the difference in porosity of all the membranes did not vary significantly in the measured range (difference not greater than 15%).

### 2.8.1 Chemical and morphological stability and thermal reliability of the phase change fibrous mat

To compare the leaking attributes between PEG and the fiber mat prepared with different PEG core flow rates, the pre-cut fiber mat and liquid PEG were placed in the freezer at  $-24 \text{ }^{\circ}\text{C}$  for 2 h. After 2 h, the sample was removed from the freezer and kept at room temperature to examine the change in the state of the sample. From Fig. S7(a), (b), it was observed that PEG at room temperature was in the liquid state, and it became solid after 2 h at  $-24 \text{ }^{\circ}\text{C}$ , signifying the phase transition phenomenon of PEG. Interestingly, the fiber mat remained intact before and after the cooling experiment. No leakage was observed after keeping all the

prepared fiber mats at  $-24 \text{ }^{\circ}\text{C}$  for 24 h (see Fig. S7(c–e)). To investigate the chemical and morphological stability of the PEG1:PC:rGO fibrous mat, the mat was kept in a freezer for 2 days at  $-24 \text{ }^{\circ}\text{C}$  and exposed at room temperature. After 10 cycles, the morphology and chemical fingerprint of the sample mat were studied via SEM and FTIR spectroscopy (see Fig. 9a, b). The SEM micrographs demonstrate the smooth fibrous network without any structural changes. The FTIR spectra of thermally cycled and as-prepared fibrous mats are similar. The characteristics of both PC and PEG FTIR peaks were present in thermally cycled fibrous mats without any shift in peak position compared to the as-prepared fibrous mat. Therefore, the collected result signifies the excellent chemical and morphological steadiness of the as-prepared fibrous mat. The thermal reliability of rGO-loaded phase change fiber was assessed via repeated heating and cooling scans performed over continuous 15 cycles using DSC. The results are shown in Fig. 9c. The indistinguishable and overlapped exothermic and endothermic DSC peaks from the second to 15th confirm the repeatability of fabricated fibers. Fig. S8 indicates an almost negligible change ( $\sim 2.79 \text{ J g}^{-1}$ ) in the melting enthalpy of the composite from second to 15th cycles. Only a  $\sim 5.36\%$  change in the PEG encapsulation ratio was observed between the second and 15th cycles of the DSC scan. The above-said observation signifies the good cyclic stability of the fiber mat.

## 3 Conclusion

In summary, we explore the effect of low molecular weight PEG in PC and rGO/PC shell-based electrospun core-shell structure towards thermal energy storage and heat transfer efficacy. Confocal microscopy confirmed two distinct natures of PEG distribution inside the PC shell. The miscibility between core and shell liquid leads to the partial mixing between core-shell architecture, as evident from XPS

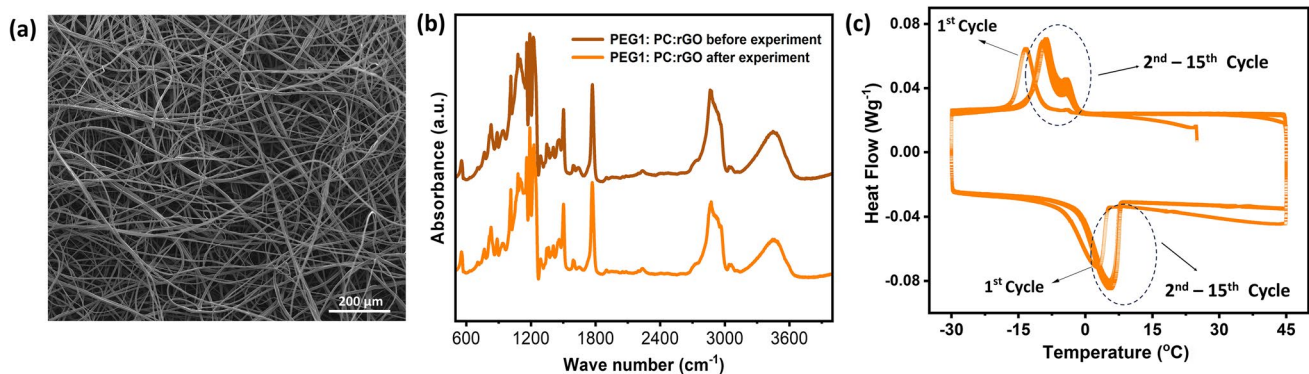


**Fig. 9** **a** SEM micrograph of PEG1:PC:rGO fiber after 10-cycle freezing–thawing experiment. **b** FTIR spectra of PEG1:PC:rGO fiber before and after 10-cycle freezing–thawing experiment. **c** DSC scan of PEG1:PC:rGO fiber up to 15 cycles

analysis. The influence of different core feed rates on the fibrous mat causes a significant difference in fiber diameter and thermal parameters of the prepared mat, as evident from SEM and DSC analysis. The prepared phase change fiber has a maximum latent melting and freezing enthalpy of  $30.1 \pm 3.7$  and  $25.6 \pm 4.0 \text{ Jg}^{-1}$  with a  $1.5 \text{ mlh}^{-1}$  core flow rate, while the rGO-loaded fiber mat maintains  $17.7 \pm 3.5 \text{ Jg}^{-1}$  and  $13.9 \pm 3.7 \text{ Jg}^{-1}$  of latent melting and freezing enthalpy with 89–90% thermal energy storage efficiency, as evaluated from the DSC result. Notably, the self-thermoregulating experiment shows that the fibrous mat can undergo a thermal buffering effect. The delay in the increase in the surface temperature is highest for the mat, which was prepared via a high core feed rate. Additionally, the presence of rGO results in an immediate rise in the surface temperature of the fibrous mat due to quick heat transport through the mat. Improved heat transfer rate by rGO, as evident from SThM measurement for individual rGO-loaded fiber, is responsible for such observation.

Furthermore, the fibrous mat demonstrates excellent non-leaking attributes, chemical and morphological stability, and efficient thermal repeatability. Therefore, the possible application area is the thermal management of PCM fibrous mat incorporated textile in a cold place and selective vaccine/medicine/food storage at near-zero temperatures ( $2\text{--}7 \text{ }^\circ\text{C}$ ).

## 4 Experimental section

### 4.1 Materials

Polycarbonate (PC) granulate was bought from Good-fellow GmbH, Germany (Makrolon 3108). Reduced graphene oxide (rGO) with a surface area  $1562 \text{ m}^2 \text{ g}^{-1}$  (size ranges from 4 to  $5 \text{ }\mu\text{m}$ ) was purchased from Nanografi Nano Technology, Germany. Polyethylene glycol (PEG) with  $M_w = 400 \text{ Da}$  was obtained from Sigma Aldrich, UK. The solvents, i.e., dimethylacetamide (DMAc) and tetrahydrofuran (THF), were procured from Sigma Aldrich, UK. The solvents and other substances were used without prior treatment or distillation.

### 4.2 Electrospinning procedure of PEG/PC microfibers

To obtain the PEG:PC core-shell structure, 24 wt.% PC was dissolved in DMAc/THF mixture at a 1:1 weight ratio under 400–500 rpm rotation speed at  $21 \pm 2 \text{ }^\circ\text{C}$ . The core-shell electrospinning fibers were obtained via coaxial electrospinning (SKE Technologies, Italy) with the climate control set to  $T = 22 \pm 1 \text{ }^\circ\text{C}$  and  $\text{RH} = 47 \pm 3\%$ . To produce PC, PEG-encapsulated PC, and rGO-loaded PEG/PC core-shell fiber, a stainless-steel coaxial nozzle with an inner core nozzle

diameter of 0.45 mm and a shell nozzle diameter of 1.4 mm was used. The samples were collected onto a stainless-steel drum collector. During the rGO:PC:PEG core-shell fibrous mat preparation, a pre-weighted amount of rGO (1 wt.% of PC amount) was first dispersed in DMAc:THF for 1 h by ultrasonication (Ultrasonic Cleaner 2.0L EMMIE20, EMAG, Poland). Then, PC granules were added to the mixture, followed by repeated ultrasonication for 2 h. Finally, the dispersed mixture was heated at  $65 \text{ }^\circ\text{C}$  until the whole PC powder was dissolved in the solution. The optimized electrospinning parameter is described in Table S1. The electrospinning was continued for 0.4–0.5 h during the production of the above-said fibrous mats.

### 4.3 Confocal light scanning microscopy (CLSM)

For the CLSM microscopy (Zeiss LSM 900, Germany) investigation, 0.125 g of Fluorescein (Chemland, Poland) was dissolved in 10-ml PEG 400 liquid via the combination of stirring at  $35\text{--}40 \text{ }^\circ\text{C}$  and ultrasonication for 30-min (EMAG Ultrasonic Cleaner 2.0L EMMIE20, Poland) process. To visualize the internal structure of core-shell fibers, a Plan-Apochromat  $63\times/1.40 \text{ Oil DIC}$  objective was used with excitation by 488 nm for fluorescein, and the detection band was 490–700 nm.

### 4.4 Surface morphology analysis

The fibrous mat's surface morphology and cross-section investigation were performed using scanning electron microscopy (SEM, Merlin Gemini II, ZEISS, Germany) at 3 kV accelerating voltage, 110 pA current, and a 4–9 mm working distance. For the cross-section study, a small portion of the sample was cut and formed into a bundle, then attached to the carbon tape. The sample coated with carbon tape was immersed in liquid nitrogen for 5 min and cut with the scalpel. Before the SEM analysis, samples were coated with an 8-nm-thick Au layer using a sputter coater (Quorum Q150RS, Quorum Technologies Ltd., UK). The fibers' diameter and fiber mat thickness were measured from SEM micrographs using ImageJ software (version 1.51, Fiji, USA). The average  $D_f$  values were evaluated from randomly selected 100 fibers. The average shell thickness of each freeze-fractured mat was evaluated from SEM micrographs using ImageJ software (version 1.51, Fiji, USA) by choosing randomly selected 50–60 freeze-fractured fibers. The surface feature of PEG1:PC and PEG1:PC:rGO fiber mat was investigated using a light microscope (Zeiss Primo Star 51) with plan achromat of  $\times 40$  objective.

### 4.5 Density

Gas pycnometer (AccuPyc 1330He, Micromeritics, Norcross, GA, USA) was used to measure the density of the

electrospun fiber mats. Before the measurement, the pre-weighted amount of fiber sample was placed in a 1-cm<sup>3</sup> cylinder cell, and the average density was calculated from 10 measurements.

#### 4.6 Wettability

The static contact angle of randomly oriented PC and core-shell PC fibers was measured by analyzing the deionized (DI) droplet (3  $\mu$ l) on the fiber surface. A DSLR camera (EOS 700D, lens EF-S 60 mm f/2.8 Macro USM, Canon, Japan) was used to take the images of water droplets after 5 s from the deposition of droplets on the samples. The wetting experiments were performed at  $T=22$  °C and RH=40%. The contact angle was measured using a drop shape analysis plug-in in ImageJ (version 1.51, Fiji, USA). About 15–20 droplets were chosen to analyze each fiber mat's standard deviation and average contact angle.

#### 4.7 FTIR measurement

The FTIR spectra of PEG were recorded on a Nicolet iS5 FT-IR spectrophotometer (Thermo Fisher Scientific, Waltham, MA, USA) by the ATR technique using diamond crystal. In contrast, the prepared fibers were recorded on the exact spectrophotometer in transmittance mode. According to Beer-Lambert law, the obtained transmittance vs. wave number data for the fibers was converted to absorbance vs. wave number data and plotted with the pristine PEG's absorbance vs. wave number data. The covered wave-number range ranged from 500 to 4000 cm<sup>-1</sup> during the measurement.

#### 4.8 XPS measurement

The XPS analyses were carried out in a PHI Versa Probe II Scanning XPS system using monochromatic Al K $\alpha$  (1486.6 eV) X-rays focused to a 100- $\mu$ m spot and scanned over the area of 400  $\mu$ m  $\times$  400  $\mu$ m. The photoelectron take-off angle was 45°, and the pass energy in the analyzer was set to 46.95 eV (0.1 eV step) to obtain high energy resolution spectra for the C 1s, O 1s, and Si 2p regions (see Fig. 3 and Fig. S5(a–i)). A dual-beam charge compensation with 7 eV Ar<sup>+</sup> ions and 1 eV electrons was used to maintain a constant sample surface potential regardless of the sample conductivity. All XPS spectra were charged in reference to the unfunctionalized, saturated carbon (C–C) C 1s peak at 285.0 eV. The operating pressure in the analytical chamber was less than  $4 \times 10^{-9}$  mbar. Deconvolution of spectra was carried out using PHI MultiPak software (v.9.9.3). Spectrum background was subtracted using the Shirley method.

### 4.9 Polymer solution conductivity measurement

The solution conductivity of PC, PC:rGO in THF:DMAc mixture, and liquid PEG was estimated using a Mettler Toledo Conductometer (Seven Compact S210, Zurich, Switzerland) connected with a conductivity probe (InLab 720). The measurements for each solution were performed three times. The ambient condition of the laboratory was  $T=23$  °C and RH=37%.

#### 4.9.1 Thermal analysis of electrospun mats

For differential scanning calorimetry (DSC) measurement, the cut pieces of each fiber mat were sealed into Mettler Toledo Al crucible before the measurements and cyclic heating-cooling from  $-25$  to  $45$  °C at a rate of  $1$  Kmin<sup>-1</sup> was performed. Then, the samples were measured using DSC (Mettler Toledo, Columbus, OH, USA), operating under a  $50$  mlmin<sup>-1</sup> nitrogen purge. The DSC scan was continued for 15 heating-cooling cycles to investigate the thermal durability test with temperature sweeping from  $-30$  to  $45$  °C at  $1$  Kmin<sup>-1</sup>. The thermal conduction behavior of PEG1:PC and PEG1:PC:rGO fibers was investigated with an atomic force microscope (AFM, CoreAFM, Nanosurf, Switzerland) equipped with scanning thermal microscopy (SThM, VertiSense™, AppNano, USA) module. The approach was adopted from a previous report [74]. VTP-375 thermal probe containing a Si cantilever with a hollow silicon dioxide tip ( $k=0.9$  Nm<sup>-1</sup>) integrated with a 50-nm thermocouple at the apex of the tip was used for measurements. The AFM laser was used to heat the cantilever tip to a stable temperature of  $\sim 60$  °C. The three different fibers for each sample were chosen randomly for measurements. The topography was obtained simultaneously with thermal data on  $30 \times 30$   $\mu$ m scan area. The scan speed was set to 3 s per line to ensure stable heat transfer between the tip and the scanned surface. The average temperature of fibers for each sample was calculated, taking only the values from the apex of the fibers to avoid false readings caused by the circular shape of the fibers. All measurements were performed in one session with the same SThM probe to ensure a similar heat transport rate from the probe and similar room conditions. The ambient conditions of the room during the experiments were RH=32–33% and  $T=23$  °C. The obtained data were processed using Gwyddion (v2.56, Gwyddion.net) and OriginPro 8 (OriginLab Corporation, USA) software. The statistical significance test of the experimental result was carried out using OriginPro 8 (OriginLab Corporation, USA) software via two sample  $T$ -test methods with a significance level 0.5.

The self-thermoregulating characteristics of all prepared fiber mats were analyzed using a thermal camera

(FLIR T560, USA). For this experiment, all the fiber mats were cut into a defined dimension (4 × 4 cm) using the laser cutter and attached to the top of the Styrofoam plate. The plate was kept inside the freezer (Amica, model number: FK3336.3DFCXAA, Poland) at  $-24 \pm 2^\circ\text{C}$  for 2 days, respectively, to ensure the thermal equilibrium between the fiber mats and the environment of the freezer, complete freezing of PCM inside the fiber mats [88]. After 2 days, the plate was exposed to room temperature, and the change in temperature of the fiber surface was measured. For the control experiment, three pieces of PC fiber mat were cut in 6 × 7 cm dimensions, attached to the Styrofoam's top surface at right, left, and middle positions, and exposed inside the freezer at  $-24 \pm 2^\circ\text{C}$  for 2 days. After 2 days, the above-said similar protocol was followed to measure the temperature distribution of the fiber mat at a definite time interval. The average temperature of each fiber surface is measured from the middle area of each fiber mat using FLIR software.

The thermal conductivity coefficient of the fiber mat was measured using FOX 50 heat flow meter (Laser comp, USA). Before the measurement, the fiber mat was cut into a round shape with a diameter of 60 mm. The gap between the two plates was set as 5 mm. Several layers of fiber mat were placed between the plates to fill the gap of the plates. The measuring surface's diameter at the plate's center was 25 mm. Pyrex glass standard was used for calibration. The temperature gradient between the hot and cold plates was set at 5 °C. The upper plate was hotter to avoid natural convection.

**Supplementary Information** The online version contains supplementary material available at <https://doi.org/10.1007/s42114-024-00934-2>.

**Author contribution** Madhurima Das—conceived of the presented idea, prepared figures, carried out the sample preparation and analysis of experimental data, performed gas pycnometry analysis, wrote the manuscript, and manuscript revision.

Daniel P. Ura—prepared figures, carried out the sample preparation and analysis of experimental data, and manuscript revision.

Piotr K. Szewczyk—prepared figures, performed SThM measurements and analysis, and manuscript revision.

Krzysztof Berniak—prepared figures, performed experiments and confocal microscopy analysis, and manuscript revision.

Joanna Knapczyk-Korczak—performed thermal conductivity measurements and analysis, performed gas pycnometry analysis, and manuscript revision.

Mateusz M. Marzec—carried out XPS experiments and analysis of the sample and manuscript revision.

Waldemar Pichór—performed thermal conductivity measurements and analysis, manuscript revision.

Urszula Stachewicz—conceived of the presented idea, wrote the manuscript, supervised the project with funding acquisition, supported needed resources, and manuscript revision.

**Funding** This study was conducted as part of the BioCom4SavEn project funded by the European Research Council under the European Union's Horizon 2020 Framework Programme for Research and Innovation (ERC grant agreement no. 948840).

**Data availability** Data will be made available on request.

## Declarations

**Competing interests** The authors declare no competing interests.

**Open Access** This article is licensed under a Creative Commons Attribution 4.0 International License, which permits use, sharing, adaptation, distribution and reproduction in any medium or format, as long as you give appropriate credit to the original author(s) and the source, provide a link to the Creative Commons licence, and indicate if changes were made. The images or other third party material in this article are included in the article's Creative Commons licence, unless indicated otherwise in a credit line to the material. If material is not included in the article's Creative Commons licence and your intended use is not permitted by statutory regulation or exceeds the permitted use, you will need to obtain permission directly from the copyright holder. To view a copy of this licence, visit <http://creativecommons.org/licenses/by/4.0/>.

## References

- Zhang Y, Umair MM, Zhang S, Tang B (2019) Phase change materials for electron-triggered energy conversion and storage: a review. *J Mater Chem A Mater* 7:22218–22228. <https://doi.org/10.1039/C9TA06678K>
- Ghiani E, Pisano G (2018) Impact of renewable energy sources and energy storage technologies on the operation and planning of smart distribution networks. In: *Operation of distributed energy resources in smart distribution networks*. Elsevier, pp 25–48. <https://doi.org/10.1016/B978-0-12-814891-4.00002-3>
- Demirhan CD, Tso WW, Powell JB et al (2020) A multiscale energy systems engineering approach for renewable power generation and storage optimization. *Ind Eng Chem Res* 59:7706–7721. <https://doi.org/10.1021/acs.iecr.0c00436>
- Song S, Zhao T, Qiu F et al (2019) Natural microtubule encapsulated phase change material with high thermal energy storage capacity. *Energy* 172:1144–1150. <https://doi.org/10.1016/j.energy.2019.02.052>
- Song S, Qiu F, Zhu W et al (2019) Polyethylene glycol/halloysite@Ag nanocomposite PCM for thermal energy storage: simultaneously high latent heat and enhanced thermal conductivity. *Sol Energy Mater Sol Cells* 193:237–245. <https://doi.org/10.1016/j.solmat.2019.01.023>
- Wang C, Wang T, Hu Z, Cai Z (2020) Facile synthesis and thermal performance of cetyl palmitate/nickel foam composite phase change materials for thermal energy storage. *J Energy Storage* 28:101179. <https://doi.org/10.1016/j.est.2019.101179>
- Report code: SRAM1865DR Phase change materials market size, share & trends analysis report by type (organic PCM, inorganic PCM, bio-based PCM), by form (encapsulated, non-encapsulated), by application (building and construction, HVAC, textiles, electronics, cold chain & packaging, thermal energy storage, others) and by region(North America, Europe, APAC, Middle East and Africa, LATAM) Forecasts, 2022–2030. <https://stratisticsresearch.com/report/phase-change-materials-market>
- Chen X, Cheng P, Tang Z, et al (2021) Carbon-based composite phase change materials for thermal energy storage, transfer, and conversion. *Adv Sci* 8: <https://doi.org/10.1002/adv.202001274>
- Shi J, Qin M, Aftab W, Zou R (2021) Flexible phase change materials for thermal energy storage. *Energy Storage Mater* 41:321–342. <https://doi.org/10.1016/j.ensm.2021.05.048>



10. Lian P, Yan R, Wu Z et al (2023) Thermal performance of novel form-stable disodium hydrogen phosphate dodecahydrate-based composite phase change materials for building thermal energy storage. *Adv Compos Hybrid Mater* 6:74. <https://doi.org/10.1007/s42114-023-00655-y>
11. Hu X, Zhu C, Wu H et al (2022) Large-scale preparation of flexible phase change composites with synergistically enhanced thermally conductive network for efficient low-grade thermal energy recovery and utilization. *Compos Part A Appl Sci Manuf* 154:106770. <https://doi.org/10.1016/j.compositesa.2021.106770>
12. Li X, Sheng M, Gong S et al (2022) Flexible and multifunctional phase change composites featuring high-efficiency electromagnetic interference shielding and thermal management for use in electronic devices. *Chem Eng J* 430:132928. <https://doi.org/10.1016/j.cej.2021.132928>
13. Cui J, Li W, Wang Y, et al (2022) Ultra-stable phase change coatings by self-cross-linkable reactive poly(ethylene glycol) and MWCNTs. *Adv Funct Mater* 32:. <https://doi.org/10.1002/adfm.202108000>
14. Wang H, Dang J, Zheng M et al (2023) High thermal storage polyurethane composite embedded with microencapsulated phase change materials and analysis of its unsteady heat transfer. *Adv Compos Hybrid Mater* 6:165. <https://doi.org/10.1007/s42114-023-00733-1>
15. Meng D, Zhao K, Zhao W, Jiang G (2017) Preparation and characterization of CA-MA eutectic/silicon dioxide nanoscale composite phase change material from water glass via sol-gel method. *J Wuhan Univ Technol -Mater Sci Ed* 32:1048–1056. <https://doi.org/10.1007/s11595-017-1709-4>
16. Wu J, Wang M, Dong L et al (2022) A trimode thermoregulatory flexible fibrous membrane designed with hierarchical core–sheath fiber structure for wearable personal thermal management. *ACS Nano* 16:12801–12812
17. Chen X, Xu J, Li Y et al (2023) Integrating multiple energy storage in 1D–2D bridged array carbon-based phase change materials. *SusMat* 3:510–521. <https://doi.org/10.1002/sus2.147>
18. Chang Y, Yao X, Chen Y et al (2023) Review on ceramic-based composite phase change materials: preparation, characterization and application. *Compos B Eng* 254:110584. <https://doi.org/10.1016/j.compositesb.2023.110584>
19. Cao Y, Weng M, Mahmoud MHH et al (2022) Flame-retardant and leakage-proof phase change composites based on MXene/polyimide aerogels toward solar thermal energy harvesting. *Adv Compos Hybrid Mater* 5:1253–1267. <https://doi.org/10.1007/s42114-022-00504-4>
20. Qin H, Pei Q-X, Liu Y, Zhang Y-W (2019) Thermal transport in graphene-based layered materials: an analytical model validated with extensive molecular dynamics simulations. *Carbon N Y* 155:114–121. <https://doi.org/10.1016/j.carbon.2019.08.062>
21. Mahmoud AED, Stolle A, Stelter M (2018) Sustainable synthesis of high-surface-area graphite oxide via dry ball milling. *ACS Sustain Chem Eng* 6:6358–6369. <https://doi.org/10.1021/acssuschemeng.8b00147>
22. Pop E, Varshney V, Roy AK (2012) Thermal properties of graphene: fundamentals and applications. *MRS Bull* 37:. <https://doi.org/10.1557/mrs.2012.203>
23. Zhang X, Li X, Zhou Y et al (2018) Enhanced thermal conductivity in a hydrated salt PCM system with reduced graphene oxide aqueous dispersion. *RSC Adv* 8:1022–1029. <https://doi.org/10.1039/C7RA10632G>
24. Chrysafi I, Avraam K, Krasia-Christoforou T (2023) Bead-free and beaded electrospun phase change fibers: a comparative study. *Eur Polym J* 191:112037. <https://doi.org/10.1016/j.eurpolymj.2023.112037>
25. Wu Y, Chen C, Jia Y et al (2018) Review on electrospun ultrafine phase change fibers (PCFs) for thermal energy storage. *Appl Energy* 210:167–181. <https://doi.org/10.1016/j.apenergy.2017.11.001>
26. Zhao L, Luo J, Li Y, et al (2017) Emulsion-electrospinning *n*-octadecane/silk composite fiber as environmental-friendly form-stable phase change materials. *J Appl Polym Sci* 134:. <https://doi.org/10.1002/app.45538>
27. Han D, Steckl AJ (2019) Coaxial electrospinning formation of complex polymer fibers and their applications. *ChemPlusChem* 84:1453–1497. <https://doi.org/10.1002/cplu.201900281>
28. Krysiak ZI, Szweczyk PK, Berniak K et al (2022) Stretchable skin hydrating PVB patches with controlled pores' size and shape for deliberate evening primrose oil spreading, transport and release. *Biomater Adv* 136:212786. <https://doi.org/10.1016/j.bioadv.2022.212786>
29. Lu Y, Xiao X, Zhan Y et al (2018) Core-sheath paraffin-wax-loaded nanofibers by electrospinning for heat storage. *ACS Appl Mater Interfaces* 10:12759–12767. <https://doi.org/10.1021/acsami.8b02057>
30. Ferapontov NB, Tokmachev MG, Gagarin AN et al (2013) Influence of the environment on swelling of hydrophilic polymers. *React Funct Polym* 73:1137–1143. <https://doi.org/10.1016/j.reactfunctpolym.2013.04.007>
31. CP Lab safety polycarbonate chemical compatibility. <https://www.calpaclab.com/polycarbonate-chemical-compatibility-chart/>. Accessed 19 Jan 2024
32. Ura DP, Knapczyk-Korczak J, Szweczyk PK et al (2021) Surface potential driven water harvesting from fog. *ACS Nano* 15:8848–8859. <https://doi.org/10.1021/acsnano.1c01437>
33. Guo Y, Ruan K, Shi X et al (2020) Factors affecting thermal conductivities of the polymers and polymer composites: a review. *Compos Sci Technol* 193:108134. <https://doi.org/10.1016/j.compscitech.2020.108134>
34. Kou Y, Wang S, Luo J et al (2019) Thermal analysis and heat capacity study of polyethylene glycol (PEG) phase change materials for thermal energy storage applications. *J Chem Thermodyn* 128:259–274. <https://doi.org/10.1016/j.jct.2018.08.031>
35. Ibrahim M, Ramadan E, Elsadek NE et al (2022) Polyethylene glycol (PEG): the nature, immunogenicity, and role in the hypersensitivity of PEGylated products. *J Control Release* 351:215–230. <https://doi.org/10.1016/j.jconrel.2022.09.031>
36. Angamma CJ, Jayaram SH (2011) Analysis of the effects of solution conductivity on electrospinning process and fiber morphology. *IEEE Trans Ind Appl* 47:1109–1117. <https://doi.org/10.1109/TIA.2011.2127431>
37. Szweczyk PK, Stachewicz U (2020) The impact of relative humidity on electrospun polymer fibers: from structural changes to fiber morphology. *Adv Colloid Interface Sci* 286:102315. <https://doi.org/10.1016/j.cis.2020.102315>
38. Ura DP, Berniak K, Stachewicz U (2021) Critical length reinforcement in core-shell electrospun fibers using composite strategies. *Compos Sci Technol* 211:108867. <https://doi.org/10.1016/j.compscitech.2021.108867>
39. Pham UHT, Hanif M, Asthana A, Iqbal SM (2015) A microfluidic device approach to generate hollow alginate microfibrils with controlled wall thickness and inner diameter. *J Appl Phys* 117:. <https://doi.org/10.1063/1.4919361>
40. Ura DP, Stachewicz U (2022) The significance of electrical polarity in electrospinning: a nanoscale approach for the enhancement of the polymer fibers' properties. *Macromol Mater Eng* 307:2100843. <https://doi.org/10.1002/mame.202100843>
41. Dror Y, Salalha W, Avrahami R et al (2007) One-step production of polymeric microtubes by co-electrospinning. *Small* 3:1064–1073. <https://doi.org/10.1002/smll.200600536>

42. Gore PM, Gawali P, Naebe M et al (2020) Polycarbonate and activated charcoal-engineered electrospun nanofibers for selective recovery of oil/solvent from oily wastewater. *SN Appl Sci* 2:1786. <https://doi.org/10.1007/s42452-020-03609-x>
43. Gupta DP, Kumar S, Kalsi PC et al (2015)  $\gamma$ -Ray modifications of optical/chemical properties of polycarbonate polymer. *World J Condens Matter Phys* 05:129–137. <https://doi.org/10.4236/wjcmp.2015.53015>
44. Kumar R, Kamakshi KM, Awasthi K (2016) Functionalized Pd-decorated and aligned MWCNTs in polycarbonate as a selective membrane for hydrogen separation. *Int J Hydrogen Energy* 41:23057–23066. <https://doi.org/10.1016/j.ijhydene.2016.09.008>
45. Kraus RG, Emmons ED, Thompson JS, Covington AM (2008) Infrared absorption spectroscopy of polycarbonate at high pressure. *J Polym Sci B Polym Phys* 46:734–742. <https://doi.org/10.1002/polb.21405>
46. Sajjan AM, Naik ML, Kulkarni AS et al (2020) Preparation and characterization of PVA-Ge/PEG-400 biodegradable plastic blend films for packaging applications. *Chemical Data Collections* 26:100338. <https://doi.org/10.1016/j.cdc.2020.100338>
47. Alemdar A, Gngr N, Ece OI, Atici O (2005) The rheological properties and characterization of bentonite dispersions in the presence of non-ionic polymer PEG. *J Mater Sci* 40:171–177. <https://doi.org/10.1007/s10853-005-5703-4>
48. Banerjee A, Blasiak B, Pasquier E et al (2017) Synthesis, characterization, and evaluation of PEGylated first-row transition metal ferrite nanoparticles as T<sub>2</sub> contrast agents for high-field MRI. *RSC Adv* 7:38125–38134. <https://doi.org/10.1039/C7RA05495E>
49. Genet M, Dupont-Gillain C, Rouxhet P (2008) XPS analysis of biosystems and biomaterials. In: *Medical applications of colloids*, pp 177–307. [https://doi.org/10.1007/978-0-387-76921-9\\_5](https://doi.org/10.1007/978-0-387-76921-9_5)
50. Pireaux JJ (1993) High resolution XPS of organic polymers: the scienta ESCA300 database. *J Electron Spectros Relat Phenomena* 62:371–372. [https://doi.org/10.1016/0368-2048\(93\)85006-7](https://doi.org/10.1016/0368-2048(93)85006-7)
51. Wagner CD, Naumkin AV, Kraut-Vass A, Allison JW, Powell CJ, Rumble JR JR Jr (2003) NIST standard reference database 20, Version 3.4 (web version). <https://srdata.nist.gov/xps/>
52. Polak M, Ura DP, Berniak K et al (2024) Interfacial blending in co-axially electrospun polymer core-shell fibers and their interaction with cells via focal adhesion point analysis. *Colloids Surf B Biointerfaces* 237:113864. <https://doi.org/10.1016/j.colsurfb.2024.113864>
53. Pei S, Ai F, Qu S (2015) Fabrication and biocompatibility of reduced graphene oxide/poly(vinylidene fluoride) composite membranes. *RSC Adv* 5:99841–99847. <https://doi.org/10.1039/C5RA19228E>
54. Zhang Y, Zhao Z, Chen J et al (2015) C-doped hollow TiO<sub>2</sub> spheres: in situ synthesis, controlled shell thickness, and superior visible-light photocatalytic activity. *Appl Catal B* 165:715–722. <https://doi.org/10.1016/j.apcatb.2014.10.063>
55. Li X, Wang L, Wang Z (2015) Radioprotective activity of neutral polysaccharides isolated from the fruiting bodies of *Hohenbuehelia serotina*. *Physica Med* 31:352–359. <https://doi.org/10.1016/j.ejmp.2015.02.004>
56. Li L, Yu H, Wang X, Zheng S (2016) Thermal analysis of melting and freezing processes of phase change materials (PCMs) based on dynamic DSC test. *Energy Build* 130:388–396. <https://doi.org/10.1016/j.enbuild.2016.08.058>
57. Paberit R, Rilby E, Ghl J et al (2020) Cycling stability of poly(ethylene glycol) of six molecular weights: influence of thermal conditions for energy applications. *ACS Appl Energy Mater* 3:10578–10589. <https://doi.org/10.1021/acsaem.0c01621>
58. Ewaldz E, Randrup J, Brettmann B (2022) Solvent effects on the elasticity of electrospinnable polymer solutions. *ACS Polymers Au* 2:108–117. <https://doi.org/10.1021/acspolymersau.1c00041>
59. Yi L, Wang Y, Fang Y et al (2019) Development of core–sheath structured smart nanofibers by coaxial electrospinning for thermo-regulated textiles. *RSC Adv* 9:21844–21851. <https://doi.org/10.1039/C9RA03795K>
60. Yazdani MR, Ajdary R, Kankkunen A et al (2021) Cellulose nanofibrils endow phase-change polyethylene glycol with form control and solid-to-gel transition for thermal energy storage. *ACS Appl Mater Interfaces* 13:6188–6200. <https://doi.org/10.1021/acsaami.0c18623>
61. Tan Y, Du X, Du Z et al (2021) Form-stable phase change composites based on nanofibrillated cellulose/polydopamine hybrid aerogels with extremely high energy storage density and improved photothermal conversion efficiency. *RSC Adv* 11:5712–5721. <https://doi.org/10.1039/D0RA10485J>
62. Min X, Fang M, Huang Z et al (2015) Enhanced thermal properties of novel shape-stabilized PEG composite phase change materials with radial mesoporous silica sphere for thermal energy storage. *Sci Rep* 5:12964. <https://doi.org/10.1038/srep12964>
63. Jin W, Jiang L, Chen L et al (2021) Enhancement of thermal conductivity by graphene as additive in lauric-stearic acid/ treated diatomite composite phase change materials for heat storage in building envelope. *Energy Build* 246:111087. <https://doi.org/10.1016/j.enbuild.2021.111087>
64. Huang X, Chen X, Li A et al (2019) Shape-stabilized phase change materials based on porous supports for thermal energy storage applications. *Chem Eng J* 356:641–661. <https://doi.org/10.1016/j.cej.2018.09.013>
65. Sun Z, Sun K, Zhang H et al (2021) Development of poly(ethylene glycol)/silica phase-change microcapsules with well-defined core-shell structure for reliable and durable heat energy storage. *Sol Energy Mater Sol Cells* 225:111069. <https://doi.org/10.1016/j.solmat.2021.111069>
66. Hu X, Huang H, Hu Y et al (2021) Novel bio-based composite phase change materials with reduced graphene oxide-functionalized spent coffee grounds for efficient solar-to-thermal energy storage. *Sol Energy Mater Sol Cells* 219:110790. <https://doi.org/10.1016/j.solmat.2020.110790>
67. Palacios A, Cong L, Navarro ME et al (2019) Thermal conductivity measurement techniques for characterizing thermal energy storage materials – a review. *Renew Sustain Energy Rev* 108:32–52. <https://doi.org/10.1016/j.rser.2019.03.020>
68. Wang H, Chu W, Chen G (2019) A brief review on measuring methods of thermal conductivity of organic and hybrid thermoelectric materials. *Adv Electron Mater* 5:. <https://doi.org/10.1002/aelm.201900167>
69. Muoz Codornu D, Moyano JJ, Belmonte M et al (2020) Thermal conduction in three-dimensional printed porous samples by high resolution infrared thermography. *Open Ceramics* 4:100028. <https://doi.org/10.1016/j.oceram.2020.100028>
70. Chen Q, Yan X, Wu L et al (2021) Small-nanostructure-size-limited phonon transport within composite films made of single-wall carbon nanotubes and reduced graphene oxides. *ACS Appl Mater Interfaces* 13:5435–5444. <https://doi.org/10.1021/acsaami.0c20551>
71. Zhu Q-H, Peng J-S, Guo X et al (2022) Accurate determination of anisotropic thermal conductivity for ultrathin composite film. *Chin Phys B* 31:108102. <https://doi.org/10.1088/1674-1056/ac6ee5>
72. Moradi A, Szewczyk PK, Stachewicz U (2023) Bridging a gap in thermal conductivity and heat transfer in hybrid fibers and yarns via polyimide and silicon nitride composites. *Small* 19:. <https://doi.org/10.1002/sml.202305104>
73. Zhang H, Zhang C, Ji W et al (2018) Experimental characterization of the thermal conductivity and microstructure of

- opacifier-fiber-aerogel composite. *Molecules* 23:2198. <https://doi.org/10.3390/molecules23092198>
74. Chen H, Daneshvar F, Tu Q, H-Jue Sue, (2022) Ultrastrong carbon nanotubes–copper core–shell wires with enhanced electrical and thermal conductivities as high-performance power transmission cables. *ACS Appl Mater Interfaces* 14:56253–56267
75. Guemann F, Pomeroy JW, Kuball M (2021) Scanning thermal microscopy for accurate nanoscale device thermography. *Nano Today* 39:101206. <https://doi.org/10.1016/j.nantod.2021.101206>
76. Teng C-C, Ma C-CM, Lu C-H et al (2011) Thermal conductivity and structure of non-covalent functionalized graphene/epoxy composites. *Carbon N Y* 49:5107–5116. <https://doi.org/10.1016/j.carbon.2011.06.095>
77. Yan Y, King SC, Li M et al (2019) Exploring the effect of porous structure on thermal conductivity in templated mesoporous silica films. *J Phys Chem C* 123:21721–21730. <https://doi.org/10.1021/acs.jpcc.9b03767>
78. Li W, Xu L, Wang X et al (2021) Phase change energy storage elastic fiber: a simple route to personal thermal management. *Polymers (Basel)* 14:53. <https://doi.org/10.3390/polym14010053>
79. Tas CE, Unal H (2021) Thermally buffering polyethylene/halloysite/phase change material nanocomposite packaging films for cold storage of foods. *J Food Eng* 292:110351. <https://doi.org/10.1016/j.jfoodeng.2020.110351>
80. Noyan ECB, Onder E, Sarier N, Arat R (2018) Development of heat storing poly(acrylonitrile) nanofibers by coaxial electrospinning. *Thermochim Acta* 662:135–148. <https://doi.org/10.1016/j.tca.2018.02.008>
81. Wang N, Chen H, Lin L et al (2010) Multicomponent phase change microfibers prepared by temperature control multifluic electrospinning. *Macromol Rapid Commun* 31:1622–1627. <https://doi.org/10.1002/marc.201000185>
82. Wan Y, Zhou P, Liu Y, Chen H (2016) Novel wearable polyacrylonitrile/phase-change material sheath/core nano-fibers fabricated by coaxial electro-spinning. *RSC Adv* 6:21204–21209. <https://doi.org/10.1039/C6RA00281A>
83. John Taylor (2001) Recommendation on the control and monitoring of storage and transportation temperatures of medicinal products. In: Medicines control agency. *Pharm J* 267(28):128–131
84. Li C, Peng M, Xie B et al (2024) Novel phase change cold energy storage materials for refrigerated transportation of fruits. *Renew Energy* 220:119583. <https://doi.org/10.1016/j.renene.2023.119583>
85. Yu X, Li Y, Wang X et al (2020) Thermoconductive, moisture-permeable, and superhydrophobic nanofibrous membranes with interpenetrated boron nitride network for personal cooling fabrics. *ACS Appl Mater Interfaces* 12:32078–32089. <https://doi.org/10.1021/acsami.0c04486>
86. Wang Z, Wang C, Gao Y et al (2023) Porous thermal insulation polyurethane foam materials. *Polymers (Basel)* 15:3818. <https://doi.org/10.3390/polym15183818>
87. Hong S-N, Yu C-J, Hwang U-S et al (2020) Effect of porosity and temperature on thermal conductivity of jennite: a molecular dynamics study. *Mater Chem Phys* 250:123146. <https://doi.org/10.1016/j.matchemphys.2020.123146>
88. Huang L, Piontek U (2017) Improving performance of cold-chain insulated container with phase change material: an experimental investigation. *Appl Sci* 7:1288. <https://doi.org/10.3390/app7121288>

**Publisher's Note** Springer Nature remains neutral with regard to jurisdictional claims in published maps and institutional affiliations.